Cortical Variability and Asymmetry in Normal Aging and Alzheimer's Disease

P.M. Thompson, J. Moussai, S. Zohoori, A. Goldkorn, A.A. Khan, M.S. Mega, G.W. Small[1], J.L. Cummings[1] and A.W. Toga

Laboratory of Neuro Imaging, Department of Neurology, Division of Brain Mapping and [1]Alzheimer's Disease Center, UCLA School of Medicine, Los Angeles, CA, USA

The onset of Alzheimer's disease (AD) is accompanied by a complex and distributed pattern of neuroanatomic change, difficult to distinguish clinically from dynamic alterations in normal aging. Extreme variations in the sulcal patterns of the human cortex have made it difficult to identify diffuse and focal variations in cortical structure in neurodegenerative disease. We report the first comprehensive 3D statistical analysis of deep sulcal structure *in vivo*, in both normal aging and dementia. High-resolution 3D T_1-weighted fast SPGR (spoiled GRASS) MRI volumes were acquired from 10 patients diagnosed with AD (NINCDS-ARDRA criteria; age: 71.9 ± 10.7 years) and 10 normal subjects matched for age (72.9 ± 5.6 years), gender, educational level and handedness. Scans were digitally transformed into Talairach stereotaxic space. To determine specific patterns of cortical variation in dementia patients, 3D average and probabilistic maps of primary deep sulci were developed for both normal and AD groups. Major sulci (including supracallosal, cingulate, marginal, parieto-occipital, anterior and posterior calcarine sulci, and Sylvian fissures) were modeled as complex systems of 3D surfaces using a multi-resolution parametric mesh approach. Variations and asymmetries in their extents, curvature, area and surface complexity were evaluated. Three-dimensional maps of anatomic variability, structural asymmetry and local atrophy indicated severe regionally selective fiber loss in AD. A midsagittal area loss of 24.5% at the corpus callosum's posterior midbody ($P < 0.025$) matched increases in structural variability in corresponding temporo-parietal projection areas. Confidence limits on 3D cortical variation, visualized in 3D, exhibited severe increases in AD from 2 to 4 mm at the callosum to a peak SD of 19.6 mm at the posterior left Sylvian fissure. Normal Sylvian fissure asymmetries (right higher than left; $P < 0.0005$), mapped for the first time in three dimensions, were accentuated in AD ($P < 0.0002$), and were greater in AD than in controls ($P < 0.05$). Severe AD-related increases in 3D variability and asymmetry may reflect disease-related disruption of the commissural system connecting bilateral temporal and parietal cortical zones, regions known to be at risk of early metabolic dysfunction, perfusion deficits and selective neuronal loss in AD.

Alzheimer's disease (AD) causes complex and distributed patterns of neuroanatomic change, which are difficult to distinguish clinically from structural alterations observed in normal aging. Extreme variations in the gyral and sulcal patterns of the human cortex make it difficult to identify group-specific variants in cortical structure, including diffuse alterations due to neurodegenerative disease. This is partly due to the lack of a precise mathematical framework for encoding and retaining information on local variability of structure across homogeneous populations (Grenander and Miller, 1994; Mazziotta *et al.*, 1995; Thompson and Toga, 1997; Thompson *et al.*, 1997). Diagnosis of AD prior to death remains one of exclusion; definitive diagnosis requires histologic findings of diffuse neuronal and synaptic loss *post mortem*, accompanied by characteristic neuropathologic lesions (McKhann *et al.*, 1984; Khachaturian *et al.*, 1985) such as β-amyloid plaques (Delaere *et al.*, 1989), neurofibrillary tangles (Wilcock and Esiri, 1982), Hirano bodies (Katzman, 1986) and granulovacuolar degeneration (Di Patre, 1990). Accurate, reproducible and practical detection and classification of anatomic differences presents considerable challenges, but holds tremendous promise in characterizing disease-related change.

Structural neuroimaging is important in the evaluation and monitoring of patients with dementia (Davis *et al.*, 1994). Computed tomography (CT) and magnetic resonance imaging (MRI) studies in AD reveal atrophy of the temporal lobe (Kido *et al.*, 1989; Erkinjuntti *et al.*, 1993; Killiany *et al.*, 1993), cortical gray matter, and caudate, lenticular and thalamic nuclei (Jernigan *et al.*, 1991), with sporadic signs of ventricular and sulcal enlargement. Early damage occurs in the entorhinal cortex (Arnold *et al.*, 1991; Braak and Braak, 1991; Gómez-Isla *et al.*, 1996), the posterior aspect of the basal nucleus of Meynert (which has strong projections to the temporal lobe; Whitehouse *et al.*, 1981), the amygdaloid nuclei (Cuénod *et al.*, 1993; Scott, 1993) and the CA1/subiculum zone of the hippocampal formation (West *et al.*, 1994). These disease-induced changes in structure often escape detection, because of complex inter-subject differences in anatomy. Identifying early neuroimaging indicators of AD has been complicated by the overlap between structural changes seen in normal aging and dementia (Friedland and Luxenberg, 1988), and controversy still exists as to whether aging and AD are dichotomous or represent a neuropathological continuum (Coleman and Flood, 1987; West *et al.*, 1994).

Cortical variation has also made it difficult to compare and integrate functional image data from multiple subjects and groups (Rademacher *et al.*, 1993; Roland and Zilles, 1994). These difficulties are compounded in dementia by additional pathologic changes. Averaging of digital brain maps, after transformation into a common 3D coordinate space, is only valid if homologous cortical regions in different subjects are brought into register. Anatomic correspondence is especially critical at functional interfaces and cytoarchitectonic boundaries, including junctional zones between adjacent microanatomic fields, most of which run along the beds and deep internal banks of major or minor cortical sulci (Sanides, 1962). Direct reference to the sulci that frame architectonic fields may present a more reliable basis for functional mapping than reference to a single standard or idealized brain (Steinmetz *et al.*, 1990; Rademacher *et al.*, 1993; Watson *et al.*, 1993).

The first 3D analysis of sulcal variability, measured in a *post mortem* population with digitally reconstructed cryosection images, found a highly heterogeneous pattern of cortical variation (Thompson *et al.*, 1996a). Despite their relevance for functional brain mapping studies in health and disease, characteristics of 3D cortical variation have not been determined *in vivo*. Superficial variations in sulcal geometry have

been reported, based on analysis of *post mortem* specimens, in primary motor, somatosensory and auditory cortex (Rademacher *et al.*, 1993), primary and association visual cortex (Stensaas *et al.*, 1974), frontal and pre-frontal areas (Rajkowska and Goldman-Rakic, 1995), and lateral perisylvian cortex (Geschwind and Levitsky, 1968; Ono *et al.*, 1990). Current quantitative information on sulcal variability *in vivo* is two-dimensional, based on 2D pneumoencephalograms (Talairach *et al.*, 1967), series of 5- or 9-mm-thick MR images (Missir *et al.*, 1989; Steinmetz *et al.*, 1989, 1990) and MR-derived surface renderings of the cortex (e.g. Vannier *et al.*, 1991). In addition to the sampling frequency limitations, these investigations represented sulci as superficial curves between the outer extremities of opposing gyri, rather than as complex 3D architectonic surfaces that merge and branch deep inside the brain.

To spatially characterize the morphometric variability in the interior surface anatomy of the brain, we modeled major sulci as complex connected systems of surfaces. A multi-resolution parametric mesh approach was used (Thompson *et al.*, 1996a,b). We selected the following primary sulci for 3D reconstruction and analysis: the supracallosal sulcus, the cingulate and marginal sulci, the anterior and posterior rami of the calcarine sulcus, the parieto-occipital sulcus, and the Sylvian fissure in both hemispheres. These 3D gyral boundaries encompass the callosal, temporo-parietal and paralimbic belts known to be at risk of bilateral atrophy in AD (Friedland and Luxenberg, 1988), as well as perisylvian regions expected to display profound structural asymmetries in normal subjects (Galaburda and Geschwind, 1981), and the parieto-occipital and calcarine surfaces of the occipital cortex, which are thought to be comparatively resistant to neuronal loss in AD (Pearson *et al.*, 1985). As major functional interfaces in the brain, these primary sulci are also easily identifiable, define gyral and lobar boundaries, and penetrate sufficiently deeply into the brain to reflect subtle and distributed variations in neuroanatomy between individuals.

Goals of this Paper

This paper has two specific goals. First, to determine specific patterns of sulcal variation in patients with AD, we developed 3D average and probabilistic maps of the primary deep sulci. Separate maps were constructed for AD patients and for elderly normal subjects matched for age, gender, educational level and handedness. These computerized 3D maps yield information on differential vulnerability of brain regions, disease-specific variants and selective changes in callosal and lobar anatomy that accompany aging and AD pathology. The maps encode the parameters of normal neuroanatomic variation, and express the coordinates and variability in location of 12 major cortical sulci in stereotaxic space. Application of the probabilistic atlasing approach (Mazziotta *et al.*, 1995; Thompson and Toga, 1998) to a diseased population results in a confidence limit, rather than an absolute representation of anatomy for each subject group. Secondly, comprehensive maps of structural asymmetry are generated, and the pronounced asymmetries of the Sylvian fissure (Geschwind and Levitsky, 1968), a region central to many investigations of functional lateralization and the neurologic basis of language function, are characterized for the first time in three dimensions. Differences in the extent, curvature, surface area and complexity of deep anatomic surfaces are quantified in health and disease. Where appropriate, results are expressed within the Talairach reference system, enabling direct reference to results of functional neuroimaging studies. The resulting framework for assessment and quantitative encoding of cortical variation reveals its regional heterogeneity, local directional biases, asymmetries and 3D characteristics in aging and dementia.

Table 1
Demographic and neuropsychiatric test data for the AD patients ($n = 10$; data courtesy of Michael Mega)

	Mean ± SD
Age (y)	71.9 ± 10.7
Sex	4M, 6F
Education (years)	13.9 ± 1.4
Mini-Mental State Exam (MMSE)[a]	19.7 ± 5.7
Trails B (s)[b]	233.9 ± 85.1
Boston naming test[c]	38.4 ± 14.2
FAS verbal fluency[d]	25.7 ± 11.9
Logical memory subscale from the WAIS-R[e]	0.3 ± 0.7
Wechsler memory scale-revised (visual reproduction[f])	0.2 ± 0.4
Rey–Osterreith complex figure completion[g]	19.8 ± 10.1
Rey–Osterreith complex figure delayed recall[g]	0.0 ± 0.0
Block design subtest from the WAIS-R[h]	6.8 ± 3.9

All values shown are raw scores, except for the Block Design subtest from the WAIS-R, for which age-corrected scaled scores are indicated.

[a]Folstein *et al.* (1975).

[b]Trailmaking Test of Executive Skills, Part B (Lezak, 1983).

[c]Kaplan *et al.* (1984).

[d]FAS: Controlled Oral Word Association Test of Verbal Fluency (Lezak, 1983).

[e]Taken from the Wechsler Adult Intelligence Scale — Revised (WAIS-R; Wechsler, 1955; Adams *et al.*, 1984).

[f]Wechsler (1955).

[g]Osterreith (1944); Rey (1941).

[h]To test visuo-constructional ability (Wechsler, 1955; Adams *et al.*, 1984).

Materials and Methods

Subjects

High-resolution 3D structural MR images were acquired from 20 subjects, matched for age, gender, educational level and handedness. The patient group included 10 subjects (mean age: 71.9 ± 10.7 years; six females/four males, all right-handed) diagnosed with AD as defined by the National Institute of Neurological and Communicative Disorders and Stroke/Alzheimer's Disease and Related Disorders Association (NINCDS-ARDRA) criteria (McKhann *et al.*, 1984). Although definitive diagnosis of AD requires direct observation of autopsy or biopsy specimens with characteristic neuropathologic lesions (McKhann *et al.*, 1984; Khachaturian, 1985), the accuracy of the NIH criteria evaluated at autopsy has been demonstrated to be 80–85% (Blacker *et al.*, 1994). Criteria for dementia included an acquired persistent decline involving at least three of the following domains: language, memory, visuospatial skills, cognition, emotion or personality (Cummings *et al.*, 1980).

In addition, the Mini-Mental State Examination (MMSE; Folstein *et al.*, 1975) was used to evaluate dementia severity. As part of a longitudinal neuropsychiatric assessment, patients underwent a comprehensive clinical evaluation which included a neuropsychological battery to assess a broad range of cognitive domains (Table 1). The AD patient group had a mean educational level of 13.9 ± 1.4 years and a mean MMSE score of 19.7 ± 5.7 (maximum score: 30), a rating comparable with values obtained in other dementia studies (Murphy *et al.*, 1993). Control subjects (mean age: 72.9 ± 5.6 years; six males/four females, all right-handed), after screening, underwent the same battery of neuropsychiatric tests, to exclude subjects with cognitive symptoms of a dementing illness. Their mean MMSE score was 28.8 ± 1.0, and they were matched with the AD subjects for age, gender, handedness and educational level (15.8 ± 2.4 years). Exclusion criteria for all subjects were the presence of a focal lesion on brain MRI, history of head trauma, past

psychiatric history or an active medical problem. Informed consent was obtained in all cases from patients and controls.

High-resolution 3D MR Image Acquisition

Three-dimensional ($256^2 \times 124$ resolution) T_1-weighted fast SPGR (spoiled GRASS) MRI volumes were acquired sagittally from the 20 subjects, on a GE Signa 1.5T clinical scanner (Milwaukee, Wisconsin) with TR/TE 14.3/3.2 ms, flip angle 35°, NEX = 1, FOV 25cm and contiguous 1-mm-thick slices (with no interslice gap) covering the entire brain. The greater slice density, combined with a high in-plane pixel resolution (0.9765 × 0.9765 mm), resulted in an improved resolution imaging matrix relative to earlier studies of aging and AD pathology [e.g. slices acquired every 5 mm (Cuénod *et al.*, 1993), or every 6 or 7 mm (Murphy *et al.*, 1993)].

Reconstruction, Normalization and Analysis

Three-dimensional image data were corrected for differences in relative position and size by transformation into standardized Talairach stereotaxic space [Talairach and Tournoux (1988); software developed at the UCLA Laboratory of Neuro Imaging, and available at: http://www.loni.ucla.edu/loni_code/loni_dist.html]. Structural brain imaging measurements, even in dementia studies (Killiany *et al.*, 1993; Murphy *et al.*, 1993), are often adjusted for normal variation in head size or brain size, to avoid confounding variance (Mathalon *et al.*, 1993). Since we regarded brain size to be an important factor in aging and AD pathology, the geometric parameters of the stereotaxic normalization were explicitly saved for analysis, allowing us to perform a coarse-to-fine morphometric analysis, at both global and local anatomical scales. At the global level, the parameters of the stereotaxic transformation were retained, to evaluate differences in brain size between the two groups. Next, the standard stereotaxic transformation was applied to the image volumes, placing them in a 3D coordinate system which compensates for these differences in overall brain size. As a result, the locations and extents of local differences in sulcal morphology, including structural asymmetries, are expressed in the Talairach reference system, enabling direct comparison with results of functional neuroimaging studies (Fox, 1995).

Subsequent anatomic analysis was conducted by operators blind to each subject's age, name and diagnostic status. Scans were analyzed only after being numerically coded and loaded in random order. Since results on anatomic asymmetry were anticipated, half of the scans from each subject group were randomly selected, and a digital transformation was applied to reflect the left and right hemispheres of the image data in the midsagittal plane. This ensured that structures were traced without knowledge of which hemisphere was being analyzed. Additional software transformed the derived surface data back into its appropriate hemisphere, prior to surface averaging and further geometric and statistical analysis.

Criteria for Delineating Sulci

Major deep sulcal fissures in the brain were reconstructed using a contour-based system. Using an interactive contouring program, all sulci were outlined manually, according to the detailed anatomic criteria set out in Steinmetz *et al.* (1989). Additional formal guidelines were devised and applied when identifying the exact course of individual sulci in three dimensions (Thompson *et al.*, 1996a).

The cellular interface between gray and white matter was used to define the opposing banks of the sulci, rather than the more diffuse boundary of gray matter at the external limit of the cortical layer. Consequently, the internal path of each sulcus was defined as the medial curve equidistant between the opposing white matter banks on either side. In rare cases, where the white matter was faint, adjacent sections were viewed for additional information. At high magnification, the outline of each sulcus was defined to be the medial axis equidistant from each bank. This contour was traced manually in all the sagittal sections in which it could be distinguished. At the external cerebral surface, the convex hull of the cortex served as an exterior limit. Figure 1 shows a sagittal projection of several sets of contours traced in the left hemisphere of one subject. Stereotaxic locations of contour points were derived from the data volume.

Surface Reconstruction from Planar Cross-sections

Interactive outlining of sulci, as described above, resulted in a sampling of ~15 000 points per sulcus. Although this dense system of points captures the details of each sulcal surface at a very local level, their spatial distribution is not quite uniform, and is arbitrarily dependent on how the sagittal sampling planes intersect the sulcus being outlined. To eliminate this dependency, we derived a standard surface representation of the same type for each sulcus. For each sulcus outlined, this algorithm generates a parametric grid of 100 × 150 uniformly spaced points that act as nodes in a regular rectangular mesh stretched over the sulcal surface. Full technical details of the mesh construction algorithm can be found in Thompson *et al.* (1996a) and Thompson and Toga (1997). Briefly, each resultant surface mesh is analogous to a regular rectangular grid, drawn on a rubber sheet, which is stretched to match all the data points. This scheme converts dense irregular systems of points, sampled during outlining, into regular parametric surfaces that can be analyzed, visualized, and compared geometrically and statistically. Under certain strict conditions, the imposition of regular grids onto biological surfaces permits cross-subject comparisons, by specifying a computed correspondence along the outline arcs and within the interior of the structures (Bookstein, 1985). For the comparisons to be valid, anatomically defined landmark points and curves must appear in

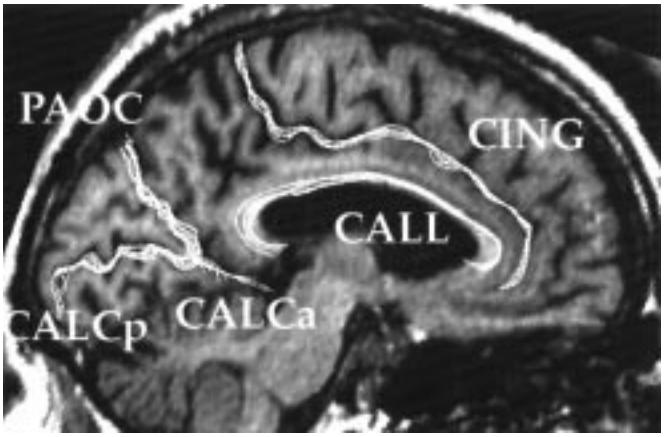

Figure 1. Sagittal projection of contours traced in the left hemisphere of a single subject. Orthogonally projected contours of the anterior and posterior rami of the calcarine sulcus (CALCa and CALCp), cingulate (CING), supracallosal (CALL) and parieto-occipital (PAOC) sulci are shown overlaid on one representative sagittal section of an Alzheimer's patient's scan. The Sylvian fissure (not shown here) was also analyzed, but is lateral to this section. Contour sets shown here were derived from the full series of sectional images spanning the left hemisphere.

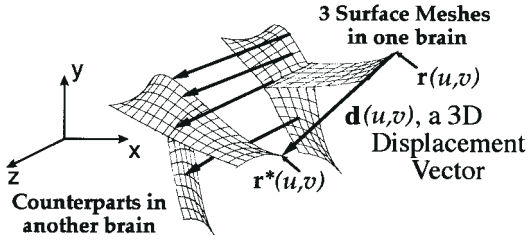

Figure 2. Scheme for matching connected systems of anatomic surfaces. Accurate detection and encoding of anatomic differences between subjects requires transformation tools that deform connected systems of mesh-based surface models (right) representing structures in one subject's anatomy, into correspondence with their counterparts (left) in the anatomy of another subject. The computation is conceptualized mathematically as a surface-based displacement map, which deforms one system of surfaces into the shape of another. Maintenance of information on surface connectivity guarantees accurate mapping of curved junctions among surfaces. Known anatomic landmarks are also used to constrain the transformation, ensuring biological as well as computational validity.

corresponding locations in each parametric grid across subjects. Figure 2 illustrates this procedure, in a case where three surface meshes in one brain are matched with their counterparts in a target brain. Exact matching is guaranteed at a 3D junction between the surfaces. Mesh partitioning strategies such as these (Thompson and Toga, 1997) ensure that known anatomic correspondences are enforced at anatomic junctions and boundaries.

Measures of Spatial Extent, Surface Curvature, Area and Fractal Dimension

Parameterization of sulcal outlines enables computation of local statistical measures and geometric parameters such as surface area, curvature indices and fractal dimension. Anterior–posterior, vertical and lateral limits, and extents of all 240 anatomical models (20 subjects, 12 parametric meshes) were determined from the digitized outlines. Surface area measures were also calculated. In addition, because one of the most prominent features of the human cerebral cortex is its high degree of convolution, normalized curvature measures were computed for all 240 sulcal surfaces. For each type of sulcus represented as a parametric mesh $\{\mathbf{r}(u,v) | 0 \le u \le I, 0 \le v \le J\}$ of fixed size $I \times J$, a simple measure of surface curvature was given by $Curv(\mathbf{r}) = \{\Sigma_{v=0 \text{ to } J} \| \mathbf{r}(I,v) - \mathbf{r}(0,v) \| \} / \{\Sigma_{v=0 \text{ to } J} \Sigma_{u=1 \text{ to } I} \| \mathbf{r}(u,v) - \mathbf{r}(u-1,v) \| \}$. This formula can be explained as follows. For any given slice in which a sulcal contour appears, the cumulative arc length, measured *along* the contour, exceeds the *direct* length of a hypothetical straight line joining the contour's endpoints. Similarly, for each of the grid lines in the *mesh*, this length excess can be expressed as a ratio which reflects the degree of inherent curvature in the surface along that grid line. The normalized curvature index, $Curv(\mathbf{r})$, is a more general ratio, which takes all grid lines into account. Its value is given by adding up the arc lengths along every grid line and dividing the total by the sum of the direct lengths of straight lines joining each of the grid lines' endpoints. Both surface area and curvature measures were defined on the parametric meshes instead of the sample points initially acquired for each sulcus.

Finally, the fractal dimension of each sulcal surface was calculated. Fractal dimension is used as an indicator of structural complexity in biological systems, ranging from bronchial and vascular trees to the cerebral cortex itself (Cressie, 1991; Stoyan and Stoyan, 1991; Griffen, 1994). The measure is severely reduced for the cortex in disorders such as epilepsy (Cook *et al.*, 1994). To evaluate the surface complexity of each structure in the AD patients and controls, an ordered hierarchy of parametric meshes $\{M_{IJ}\}$ was generated for each sulcus S, with variable resolution $I \times J$ (I = 2 to 100). If $A\{M_{IJ}\}$represents the surface area of the mesh M_{IJ}, S has fractal dimension $Dim_F(S) = 2 - \{\partial \ln A\{M_{IJ}\}) / \partial \ln(1/I)\}$. The gradient of the associated multifractal plot was obtained by least squares regression of the function $\ln A\{M_{IJ}\}$ against $\ln(1/I)$, over the range $2 \le I \le 100$. This procedure was repeated for all 240 meshes.

Surface Averaging and Local Variability Measures

The relationship between two sulci of the same type was represented as a map which displaces one surface mesh onto another in stereotaxic space (Fig. 2). For each and every point on a surface mesh M_1, and every point on a similar mesh M_2, the two points were matched if they had the same grid location within their respective surfaces. For each such association, the discrepancy was computed as a 3D displacement vector between corresponding nodal points. When mapping a parametric grid from one sulcal surface $\mathbf{r}^{(1)}(u,v)$ to its counterpart in another brain $\mathbf{r}^{(2)}(u,v)$, a second criterion was enforced. This criterion ensured that the amount of local stretching or contraction of the grid that resulted from the mapping process, represented by the scalar field

$$\theta(u,v) = [\, \| \partial \mathbf{r}^{(2)}(u,v)/\partial u \| \times \| \partial \mathbf{r}^{(2)}(u,v)/\partial v \| \,] / [\, \| \partial \mathbf{r}^{(1)}(u,v)/\partial u \| \times \| \partial \mathbf{r}^{(1)}(u,v)/\partial v \| \,]$$

was uniform across the whole surface. The resulting correspondence field $\mathbf{r}^{(1)}(u,v) \rightarrow \mathbf{r}^{(2)}(u,v)$ between surfaces was therefore unaffected by, and entirely independent of, any global translational or rotational shifts of one surface relative to the other (Thompson *et al.*, 1996a). Ultimately, this procedure yielded a full displacement map for every pair of sulcal surfaces of the same type.

For both the normal elderly and AD groups, an average surface representation was derived, together with local measures of group variability for each sulcal type, by averaging the 3D position vectors of corresponding nodes across all 10 subjects in each group. Local measures of spatial variance were based upon the availability of this average surface representation, together with the concept of a *displacement map* (Fig. 2). A complete mathematical formulation of this notion can be found in Thompson *et al.* (1996b, 1997) and Thompson and Toga (1997).

Confidence Limits for Cortical Regions in Stereotaxic Space

To quantify local variations in brain structure, confidence regions for the location of sulcal points in stereotaxic space were determined. For each subject group, these represent regions of stereotaxic space in which a specific sulcal point is likely to fall with probability α, where α is any desired confidence threshold. Briefly, if $\mathbf{r}^{(1)}(u,v)$, $\mathbf{r}^{(2)}(u,v)$ . . . $\mathbf{r}^{(N)}(u,v)$ are 3D locations of sulcal surface points indexed by mesh coordinates (u,v) in N separate individuals, the 3D dispersion of these anatomic points around their mean location $\mathbf{r}_\mu(u,v) = (1/N)\Sigma \mathbf{r}^{(i)}(u,v)$ is indicated by the set of 3D displacement vectors $\mathbf{d}^{(i)}(u,v) = \mathbf{r}^{(i)}(u,v) - \mathbf{r}_\mu(u,v)$. As shown elsewhere (Thompson and Toga, 1997), if $\mathbf{d}^{(i)}(u,v)$ has the multivariate normal density on $\mathbb{R}^3$ with non-stationary covariance tensor $\Psi(u,v)$, then for any desired confidence threshold α, $100(1 - \alpha)\%$ *confidence regions* in stereotaxic space, in which a point corresponding to $\mathbf{r}_\mu(u,v)$ will occur *with probability* α in a randomly selected subject, are given by nested ellipsoidal regions

$$\mathbf{E}_{\lambda(\alpha)}(\mathbf{x}) = \{\mathbf{p} \,|\, [\mathbf{p} - \mathbf{r}_\mu(u,v)]^T [\Psi(\mathbf{x})]^{-1} [\mathbf{p} - \mathbf{r}_\mu(u,v)] < \lambda(\alpha)\}$$

where $\lambda(\alpha) = [N(N-3)/3(N^2-1)]^{-1} F_{\alpha,3,N-3}$, and $F_{\alpha,3,N-3}$ is the critical value of the F distribution with 3 and $N - 3$ degrees of freedom such that $\Pr\{F_{3,N-3} \ge F_{\alpha,3,N-3}\} = \alpha$.

Three-dimensional Variability Maps

Profiles of variation from the average surfaces, for the Alzheimer's and control subjects, were derived locally across the surface of each anatomic structure. If $\mathbf{r}^{(i)}(u,v)$ is the 3D position in stereotaxic space of the point with parametric coordinates (u,v) on the ith person's mesh, then the vector displacement map $\mathbf{d}^{(i)}(u,v) = \mathbf{r}^{(i)}(u,v) - \mathbf{r}_\mu(u,v)$ expresses the ith surface's local deviation from an 'average mesh', derived from all the subjects in the group. This map assigns a 3D displacement vector to each internal surface point. The root mean square (r.m.s.) magnitude of these displacements, in the N surface maps $\mathbf{d}_i$ from average to individual, provides a measure of that surface's variability in stereotaxic space. The values of this function are in millimeters of stereotaxic space. Profiles of local variability were visualized (using Data Explorer 2.1, IBM Visualization Software), as they varied across each anatomic surface, by color-coding the surface representation of each sulcus.

Regional Analysis of Corpus Callosum Morphology

To determine whether there was a regionally selective pattern of callosal change accompanying AD pathology, the morphology of the callosum at the mid-sagittal plane was analyzed by partitioning it into five regions, according to the strategy developed by Duara *et al.* (1991; see also Larsen *et al.*, 1992). Although other effective partitioning and analysis schemes exist (Clarke *et al.*, 1989; Witelson, 1989; Hynd *et al.*, 1995; Davatzikos *et al.*, 1996), this regime is relatively simple to apply clinically, and digitally divides the anterior–posterior extent of the callosum into fifths, the anterior and posterior of which approximately represent the genu and splenium respectively. This results in a segregation of callosal fibers belonging to distinct cortical regions, since the topographic organization of callosal fibers, in relation to the cortical regions they connect, enables the construction of a map of cortical regions along the callosum (Pandya and Seltzer, 1986). The cross-sectional area of each of these five callosal subdivisions was determined for all 20 subjects, both before and after transformation of the image data into Talairach stereotaxic space.

Statistical Tests

In addition to the surface maps of statistics on local variability, confidence limits and structural asymmetry in three dimensions, two types of statistical comparisons were planned and carried out between groups: (i)

comparisons of means from AD subjects and controls, using unpaired Student's *t*-tests, for specific structural parameters (e.g. regional callosal area and parameters of the stereotaxic transform as indices of regional atrophy); and (ii) comparisons between hemispheres, using paired *t*-tests, in both controls and AD subjects, to assess anatomic asymmetry. To control for multiple group comparisons, Bonferroni's correction was applied.

All 3D reconstruction programs were written in C and executed on DEC Alpha AXP3000 workstations running OSF-1.

Results

From the broad spectrum of neuroanatomic variables examined here, numerous trends were clear. Global patterns of atrophy and variation, such as widespread reductions in brain volume, are described first. We proceed to a more local analysis of the typical patterns of cortical variation in three dimensions. Finally, spatial profiles of anatomic asymmetries are analyzed for each subject group, and disease-specific alterations in specific sectors of the Sylvian fissures, temporo-parietal cortex and corpus callosum are investigated.

Patterns of Global and Regional Atrophy in AD

The geometric parameters of the stereotaxic normalization (Talairach and Szikla, 1967) were retained for analysis, allowing volume comparisons between groups for 12 brain sectors defined by the Talairach system (Table 2; see legend for definitions of specific brain sectors). A significant 8.2% volume loss in AD subjects relative to controls was observed in the central sector, falling from 438.6 ± 14.3 cm^3 in controls (mean ± SEM) to 402.6 ± 13.1 cm^3 in the AD group ($P < 0.05$). In the lower central sector, a region lying below the anterior commissure–posterior commissure (AC–PC) line and between the anterior and posterior commissures, a 9.3% volume reduction was observed in AD compared with age-matched controls (falling from 165.4 ± 5.1 cm^3 to 150.1 ± 4.8 cm^3; $P < 0.05$). This volume reduction represented the combined effect of three linear factors: (i) a bilateral atrophy of the cerebral hemispheres, whose width fell by 2.5% on the left (from 67.7 ± 0.7 mm in controls to 66.0 ± 0.9 mm in AD) and by 3.0% on the right (from 66.7 ± 0.8 mm in controls to 64.7 ± 0.9 mm in AD); (ii) a 3.6% reduction in the AC–PC distance from 28.5 ± 0.7 mm in controls to 27.5 ± 0.4 mm in the AD group; and (iii) a 3.1% decrease in the vertical distance of the temporal lobe tip from the AC, falling from 43.2 ± 0.6 mm in controls to 41.8 ± 0.9 mm in the AD group. While sector volumes only indirectly reflect cerebral atrophy, and are not conventional neuroimaging indicators of dementia, it was notable that the central sector volume, which can be calculated rapidly, still differentiated the two subject groups ($P < 0.05$).

Striking trends were also revealed when specific neuroanatomic indices, calculated for each subject group, were compared with their reference values prescribed by the Talairach system (Talairach and Szikla, 1967; Talairach and Tournoux, 1988). Extents of the brain along the three orthogonal axes, prior to stereotaxic transformation, the combined volume of all 12 brain sectors and the internal AC–PC distance were analyzed by a two-tailed *t*-test, to identify group departures from canonical values. Strict Bonferroni criteria were applied and planned comparisons were enforced to control for Type I error (Table 3). In the AD patients, the mean rostro-caudal and lateral extents of the brain (165.2 ± 2.0 and 130.7 ± 1.7 mm respectively) were significantly depressed when compared with their reference values ($P < 0.05$, after Bonferroni correction). By contrast, in age-matched controls, neither rostro-caudal, lateral nor vertical extents of the brain were significantly different from their respective reference values (166.4 ± 3.1, 134.4 ± 1.7 and 114.4 ± 1.1 mm; all $P > 0.05$). In addition, while the combined volume of all 12 brain sectors was not significantly different from its reference value of 2773.0 cm^3 in controls (2562.3 ± 78.6 cm^3; $P > 0.05$), the same measure in the group of Alzheimer's patients was significantly reduced (2424.6 ± 83.4 cm^3; $P < 0.05$ after Bonferroni correction; $P < 0.005$ uncorrected).

Table 2
Regional cerebral volume indices in AD and normal aging

Region	Controls (cm^3)	AD (cm^3)	AD volume reduction (%)
Total cerebral volume index[a] (cm^3)	2562.3 ± 78.6	2424.6 ± 83.4	5.4
(as % of Talairach reference brain[b])	(92.4% ± 2.8%)	(87.4% ± 3.0%)	
Specific brain sectors[c]			
Frontal	994.2 ± 32.4	960.2 ± 44.1	3.4
	(88.6% ± 2.9%)	(85.6% ± 3.9%)	
Parieto-occipital	1129.5 ± 42.5	1062.0 ± 30.4	6.0
	(88.6% ± 3.3%)	(83.3% ± 2.4%)	
Central	438.6 ± 14.3	402.6 ± 13.1	8.2 (**$P < 0.05$)
	(116.4% ± 3.8%)	(106.9% ± 3.5%)	

Specific brain sectors defined by the Talairach stereotaxic reference system exhibited pronounced volume reductions in AD relative to age-matched control subjects.

[a]While volumes of these sectors are not measures of tissue volume *per se*, the central sector volume still differentiated the two subject groups ($P < 0.05$). As a product of three simple linear measures, this index may be more readily calculated than cerebral volume, offering a convenient index of disease-specific tissue loss in three dimensions. When the central sector is further partitioned into *upper* and *lower* sectors, lying above and below the AC–PC line respectively, volume loss due to AD in the lower central sector reached 9.3%, and only two control subjects had a sector volume below while only two AD subjects had a sector volume above (158 cm^3). Sector volumes are expressed here in cm^3 (as a mean ± SEM for each subject group)

[b]Sector volumes expressed as a percentage (shown in parentheses) of corresponding sector volumes for the Talairach standard reference brain, which forms the basis of the internationally accepted stereotaxic reference system for human functional neuroimaging studies (Fox, 1995).

[c]Regions are defined as follows: a rotational alignment of the image volume horizontally orients the line connecting anterior and posterior commissures (AC–PC line) and vertically orients the interhemispheric plane. A rectangular bounding box is defined around the brain tissue, and in this box regions anterior to the AC and posterior to the PC are designated *frontal* and *parieto-occipital* respectively, with a *central* region lying between the two commissures.

Despite considerable inter-subject variation, the Talairach system served as a statistically acceptable approximation to the linear brain dimensions of the elderly control group (q.v., Table 3). The sole exception was that the intercommissural AC–PC distance was greater in both subject groups ($P < 0.05$) than the standard value of 23.5 mm established by Talairach, reaching values of 27.5 ± 0.4 mm in the AD group and 28.5 ± 0.7 mm in controls.

Three-dimensional Variability Maps in Aging and AD

When confidence regions were computed for normal subjects' cortical regions in stereotaxic space, striking local trends came to light (Fig. 3). First, indices that reflected the overall magnitude of variability for a sulcal surface were remarkably consistent from one sulcus to another (Table 4). In the control group, the mean 3D deviation of individual sulci from the average surface representation of sulcal anatomy was in the 6.1–8.3 mm range for all structures except the corpus callosum, whose 3D deviation from the mean averaged only 4.0 mm in both hemispheres and fell to a low point of 2.8 mm at the inferomedial limit of the splenium. However, these summary measures of variability disguised the extremely heterogeneous profiles of variability across the surfaces of individual sulci (Fig. 3). As observed in preliminary *post mortem* studies (Thompson *et al.*,

Table 3
Three-dimensional neuroanatomic indices in aging, AD and the Talairach stereotaxic system

Measurement	Talairach reference value	Controls (%)	AD (%)
Linear measures (mm)			
Total rostral extent	173.0	96.2 ± 1.8‡	95.5 ± 1.1**
AC–PC distance	23.5	121.2 ± 2.8***	116.8 ± 1.7***
AC to frontal limit	70.0	92.1 ± 1.5	93.2 ± 1.9
PC to occipital limit	79.5	92.3 ± 2.9	91.2 ± 1.5
Total vertical extent	117.0	97.8 ± 1.0‡	95.7 ± 1.8‡
Above AC–PC line	74.5	95.6 ± 1.6	94.2 ± 1.9
Below AC–PC line	42.5	101.5 ± 1.4	98.3 ± 2.0
Total lateral extent	137.0	98.1 ± 1.0‡	95.4 ± 1.3**
Left hemispheric width	68.5	98.9 ± 1.0	96.4 ± 1.4
Right hemispheric width	68.5	97.3 ± 1.1	94.4 ± 1.4
Brain sector volumes (cm^3)			
All brain sectors combined	2773.0	92.4 ± 2.8‡	87.4 ± 3.0**
Upper frontal	714.5	86.8 ± 3.4	84.3 ± 4.0
Lower frontal	407.6	91.8 ± 2.5	87.9 ± 4.0
Upper parieto-occipital	811.4	86.7 ± 3.5	82.1 ± 2.5
Lower parieto-occipital	462.9	92.1 ± 3.6	85.4 ± 2.5
Upper central	239.9	113.9 ± 4.2	105.2 ± 3.6
Lower central	136.8	120.9 ± 3.7	109.7 ± 3.5

Striking trends were revealed when specific neuroanatomic indices, calculated for each subject group, were compared with their reference values prescribed by the Talairach system (Talairach and Szikla, 1967; Talairach and Tournoux, 1988). Extents along the three orthogonal axes prior to stereotaxic transformation, the resulting index of cerebral volume and the internal AC–PC distance were analyzed by a two-tailed *t*-test to identify group departures from canonical values. Measures are expressed here as a percentage of the standard parameters for the Talairach reference brain (mean ± SEM for each subject group). Strict Bonferroni criteria were applied and planned comparisons were enforced to control for Type I error. Only comparisons planned in advance (indicated by symbols) were therefore evaluated statistically. In the AD patients, the mean rostro-caudal and lateral extents of the brain, as well as the resulting combined volume of all 12 brain sectors were significantly depressed when compared with their reference values ($P < 0.05$, even after Bonferroni correction for multiple comparisons). By contrast, in age-matched controls, neither the combined volume nor the rostro-caudal, lateral or vertical extents of the brain were significantly different from their respective reference values (all $P > 0.05$). Note the considerably greater value of the intercommissural AC–PC distance in both subject groups than the standard value of 23.5 mm established by Talairach. This disparity underscores the need to develop more flexible atlas systems which explicitly reflect the anatomy of different population subgroups, based on an empirical analysis and 3D encoding of group-specific patterns of neuroanatomic variation (Mazziotta *et al.*, 1995; Thompson and Toga, 1997; Thompson *et al.*, 1997).

**Significantly decreased, $P < 0.05$ (after Bonferroni correction), relative to Talairach reference value.

***Significantly larger, $P < 0.005$ (after Bonferroni correction), than Talairach reference value.

‡Not significantly different ($P > 0.05$).

Table 4
Sulcal variability expressed as a 3D distance in stereotaxic space

Structure	Controls (mm)	AD (mm)
Left hemisphere		
CALCa	6.4 ± 0.3	7.2 ± 1.0
CALCp	8.6 ± 1.2	6.1 ± 1.0
CALL	3.7 ± 0.4	4.0 ± 0.7
CING	8.3 ± 0.7	5.3 ± 0.9
PAOC	6.1 ± 0.9	5.9 ± 0.8
SYLV	7.1 ± 0.8	9.1 ± 2.6
Right hemisphere		
CALCa	6.2 ± 0.4	6.9 ± 0.7
CALCp	7.1 ± 1.0	6.7 ± 0.9
CALL	4.3 ± 0.5	4.1 ± 0.9
CING	8.3 ± 1.8	7.6 ± 1.4
PAOC	6.7 ± 0.8	6.5 ± 0.5
SYLV	7.2 ± 2.0	5.9 ± 0.8
Cerebral aqueduct	2.9 ± 0.7	2.6 ± 0.4

This summary measure of variability is obtained as follows. The map which displaces the sulcal surface in a given subject onto the average representation for that sulcus assigns a 3D displacement vector to each node in that subject's surface. Within each subject group, comparison of the 10 individual surface maps yields a variance value for the magnitude of the displacement vector assigned by each map to a given node. The square root of this measure gives the positional SD of each node as a distance in stereotaxic space. The mean and SD of these nodal values are shown here for each sulcus. This final numeric value gives a global indication of the stereotaxic variability of each sulcus, when all the nodes on its surface are taken into account. Values are in mm of Talairach stereotaxic space. The floor of the cerebral aqueduct (III) was also included as a control structure, expected to display minimal variability. These summary measures are similar in both AD and control groups, and their values disguise the highly heterogeneous profile of variability across the surface of individual structures (cf. Figs 3, 4).

1996a), local variability was consistently higher towards the exterior cortical surface. For the parieto-occipital, posterior calcarine, cingulate sulci and Sylvian fissures in both brain hemispheres, confidence limits on 3D variation increased dramatically from an SD of 2–4 mm internally to a peak of 12–13 mm at the exterior cerebral surface. By contrast, however, variability at the superior callosal surface and at the floor of the cerebral aqueduct (which was included as a control structure, expected to show minimal variability) never exceeded an SD of 5.7 and 4.4 mm respectively, although variability at the aqueduct rose slightly with increasing distance from the posterior commissure (correlation coefficient $r = 0.95$ in both controls and AD).

These regional phenomena are not surprising, given that the Talairach system fixes the locations of the two commissures, and is accordingly more effective at reconciling population variances close to these control points. In particular, for the posterior calcarine sulci, the measure of 3D r.m.s. variability rose in controls at an estimated rate of 0.11 mm per mm distance from the PC on the left ($r = 0.89$) and 0.08 mm per mm from the PC on the right ($r = 0.86$). AD patients displayed similarly striking increases in cortical variability towards the exterior cerebral surface, rising to a slightly higher peak value (10.9 mm) than that seen in controls (10.1 mm). Local variability rose at a rate of 0.08 mm per mm from the PC on the left ($r = 0.79$) and 0.06 mm per mm from the PC on the right ($r = 0.72$). Sulcal variability in the occipital lobe as a whole was more strongly correlated with 3D distance from the PC in controls ($r = 0.62$) than in AD ($r = 0.13$), perhaps reflecting a secondary process of disease-related atrophy in neighboring parietal areas.

More surprising was the high degree of variability found in the deep anterior cingulate (SD: 11.7 mm) and the pronounced increase in variability towards the posterior limits of the Sylvian fissures (rising sharply from an SD of 5.9 mm rostrally to 12.0 caudally on the left and from 4.8 mm rostrally to 12.1 mm caudally on the right). Sharp increases in local variability in these anterior limbic and posterior temporal zones may be attributable to multiple branching patterns, and variations in the incidence and topology of neighboring accessory gyri (Galaburda and Geschwind, 1981; Ono *et al.*, 1990; Leonard, 1996; Paus *et al.*, 1996a,b).

Alzheimer's Disease

Three-dimensional variability maps constructed for the same regions in the group of Alzheimer's subjects largely corroborated these control observations (Fig. 4). This time, however, confidence limits on 3D variation showed an extraordinary increase from an SD of 2.2–6.1 mm internally at the corpus callosum to a peak of 19.6 mm at the posterior limit of the left Sylvian fissure. As found in the control group, variability at the superior callosal surface and at the floor of the cerebral aqueduct never exceeded an SD of 6.1 and 3.7 mm respectively, while the variability across the surface of the Sylvian fissure rose extremely sharply from an SD of 6.0 mm rostrally to 19.6 mm caudally on the left and from 5.0 mm rostrally to 9.0 mm caudally

on the right. A similarly remarkable variation characterized the anterior cingulate region, which, despite its close proximity to the relatively invariant tip of callosal genu (SD: ~3.5–3.8 mm), displayed extreme positional variation in stereotaxic space (SD: 8–10 mm; see Fig. 4).

Comparison with Cryosectioned Subjects

Cross-modality effects on measures of 3D cortical variation were investigated by comparing MR-derived variability maps with those obtained in previous studies of normal elderly brains imaged immediately *post mortem* by ultra-high-resolution digital cryosection imaging (Thompson *et al.*, 1996a). Figure 5 shows occipital lobe variability maps for the 10 normal elderly subjects (top left) and 10 Alzheimer's patients (top right) imaged by high-resolution MRI in the current study, as well as (bottom left) identically derived maps for the six cryosection subjects analyzed in Thompson *et al.* (1996a). While the characteristic rise in variability towards the exterior cerebral surface was a universal phenomenon, the peak variability values obtained across population subgroups differed substantially. As expected, the high cortical variability in 3D MRI was compounded by additional factors (e.g. cryoprotection, CSF loss and fixation) that affect specimen integrity in *post mortem* studies.

Three-dimensional Asymmetry Maps in Aging and AD

Striking regional trends became apparent when 3D maps of structural asymmetry were constructed for deep sulcal surfaces in both subject groups. Figure 6 shows a color-coded digital map of sulcal asymmetry in three dimensions, highlighting its local biases on an average surface representation of the normal elderly group's anatomy. Note the negligible asymmetry (0.0–2.3 mm) of the callosal surface, and the mild asymmetry values for parieto-occipital, anterior and posterior calcarine and cingulate sulci (0.1–3.0, 1.0–4.3, 0.9–4.4 and 0.6–4.6 mm respectively). Values obtained for these relatively symmetric structures are in marked contrast with the severe asymmetry exhibited by the Sylvian fissure (0.8–15.4 mm).

As is apparent from the 3D average surface representations of anatomy in both normal aging (Fig. 3) and AD (Fig. 4), the Sylvian fissure is significantly longer and more horizontal on the left than on the right (Geschwind and Levitsky, 1968; Witelson and Kigar, 1992; Galaburda, 1995). The right Sylvian fissure also shows a pronounced upward turn at its posterior limit (Figs 3–6). Among the many functionally important areas on the lateral perisylvian surface, the planum temporale (a planar cortical field located on the posterior floor of the Sylvian fissure) closely corresponds to auditory association area Tpt, which represents a critical part of the language representation of the left hemisphere and has a volume up to seven times larger on the left than on the right (Galaburda *et al.*, 1978). Consistent with these cytoarchitectural considerations, the posterior limit of the right Sylvian fissure was found, in controls, at a mean stereotaxic position of $Y = -31.6 \pm 1.8$ mm (i.e. 31.6 mm caudal to the origin of stereotaxic space at the anterior commissure), while the left Sylvian fissure extended another 9.7 mm further back to a mean location, for the caudal limit, at $Y = -41.3 \pm 2.1$ mm. Asymmetry was therefore substantial in controls ($P < 0.0005$). In AD, this asymmetry was accentuated (with $P < 0.0002$): while the right posterior terminus was found at mean stereotaxic position $Y = -31.9 \pm 1.1$ mm, a value which almost exactly matched its location in controls, the left posterior limit was found 16.6 mm more caudally at $Y = -48.5 \pm 3.5$ mm. Comparative analysis of the 3D variability and asymmetry maps in health and disease (Figs 3, 4, 6, 7) suggested that both the variability and asymmetry at the left posterior limit are far greater in AD than in controls, with local asymmetry reaching a highly elevated value of 21.8 mm in AD compared with only 15.4 mm in controls. Between-hemisphere differences in the anterior–posterior position of the Sylvian fissure's posterior limit were also found to be significantly greater in AD than in matched controls ($P < 0.05$).

Figure 3. Three-dimensional variability maps and average surface representation for 12 major sulci in elderly normal subjects. Three-dimensional average surface representations are shown for all 12 deep sulci from corresponding hemispheres of the 10 elderly normal subjects' brains in Talairach stereotaxic space. The floor of the cerebral aqueduct (CAQD) was included as a control structure, expected to display minimal intersubject variability. Local variability is shown (in color) on an average surface representation of each sulcus. The color encodes the root mean square magnitude of the displacement vectors required to map the surfaces from each of the 10 subjects onto the average, according to standard parametric criteria. Notice the pronounced increase in variability towards the posterior Sylvian and exterior occipital surface. The highly variable cingulate sulcus contrasts sharply with the relatively invariant corpus callosum lying inferior to it.

Figure 4. Three-dimensional variability maps and average surface representation for 12 major sulci in patients with AD. Identically constructed 3D average surface representations and variability maps are shown for the 12 major sulci (and aqueductal floor) in the 10 Alzheimer's patients. Notice this time the extraordinary increase in variability from an SD of 2.2–6.1 mm internally at the callosum to a peak of 19.6 mm at the posterior limit of the Sylvian fissure. Metabolic dysfunction in temporoparietal association cortex, assessed with positron emission tomography (PET), appears early in AD (Friedland *et al.*, 1985), and these data are consistent with the hypothesis that AD pathology severely disrupts temporo-parietal anatomy. The extent of this variation is important to recognize in functional neuroimaging studies of dementia, since averaging and stereotaxic subtraction of functional maps may lead to spurious results due to anatomic (rather than functional) differences between groups (Meltzer and Frost, 1994; Woods, 1996). Atrophy and degeneration of the perisylvian region may widen the Sylvian fissure, adding variation and asymmetry to the structural patterns of normal aging. These effects are further investigated in Figs 5–7.

Figure 6. Three-dimensional maps of structural asymmetry in the deep surface anatomy of elderly normal subjects. A local index of anatomic asymmetry in different brain regions is shown here (overlaid in color) on an average 3D surface representation of deep sulci in normal elderly subjects. Average structures were digitally mapped into the opposite hemisphere by reflection in the mid-sagittal plane of Talairach stereotaxic space. Three-dimensional displacement vector maps (Fig. 2) were then calculated according to the parametric criteria described earlier. These maps express the residual spatial mismatch (or local anatomic asymmetry) between each structure and its reflected counterpart. The magnitude of this displacement, which provides an index of anatomic asymmetry in different brain regions, was then encoded in color on an average 3D surface representation of each group's anatomy. Negligible asymmetry (0.0–2.3 mm) at the callosal surface contrasts sharply with the severe Sylvian fissure asymmetry (0.8–15.4 mm). The profile of Sylvian fissure asymmetry in 3D space suggests that although the fissure exhibits a higher upswing on the right than the left, this asymmetry is restricted to the posterior limit of the structure. This is consistent with prior observations that the planum temporale, a planar cortical field located on the posterior floor of the Sylvian fissure, has a volume up to seven times larger and extends farther posteriorly on the left than on the right (Galaburda *et al.*, 1978).

Figure 7. Three-dimensional maps of structural asymmetry in the deep surface anatomy of patients with AD. Identically constructed variability maps are shown on the average 3D surface representation of the 12 major sulci in AD. Note this time the extraordinary increase in asymmetry in AD to a peak value of 21.8 mm at the posterior limit of the Sylvian fissure, which compares with a peak value of only 15.4 mm in controls (Fig. 6). Disease-related disruption of temporo-parietal regions, which are at risk of early metabolic dysfunction, perfusion deficits and early neuronal loss in AD, may constitute a source of secondary anatomic variation and asymmetry superimposed on that seen in normal aging.

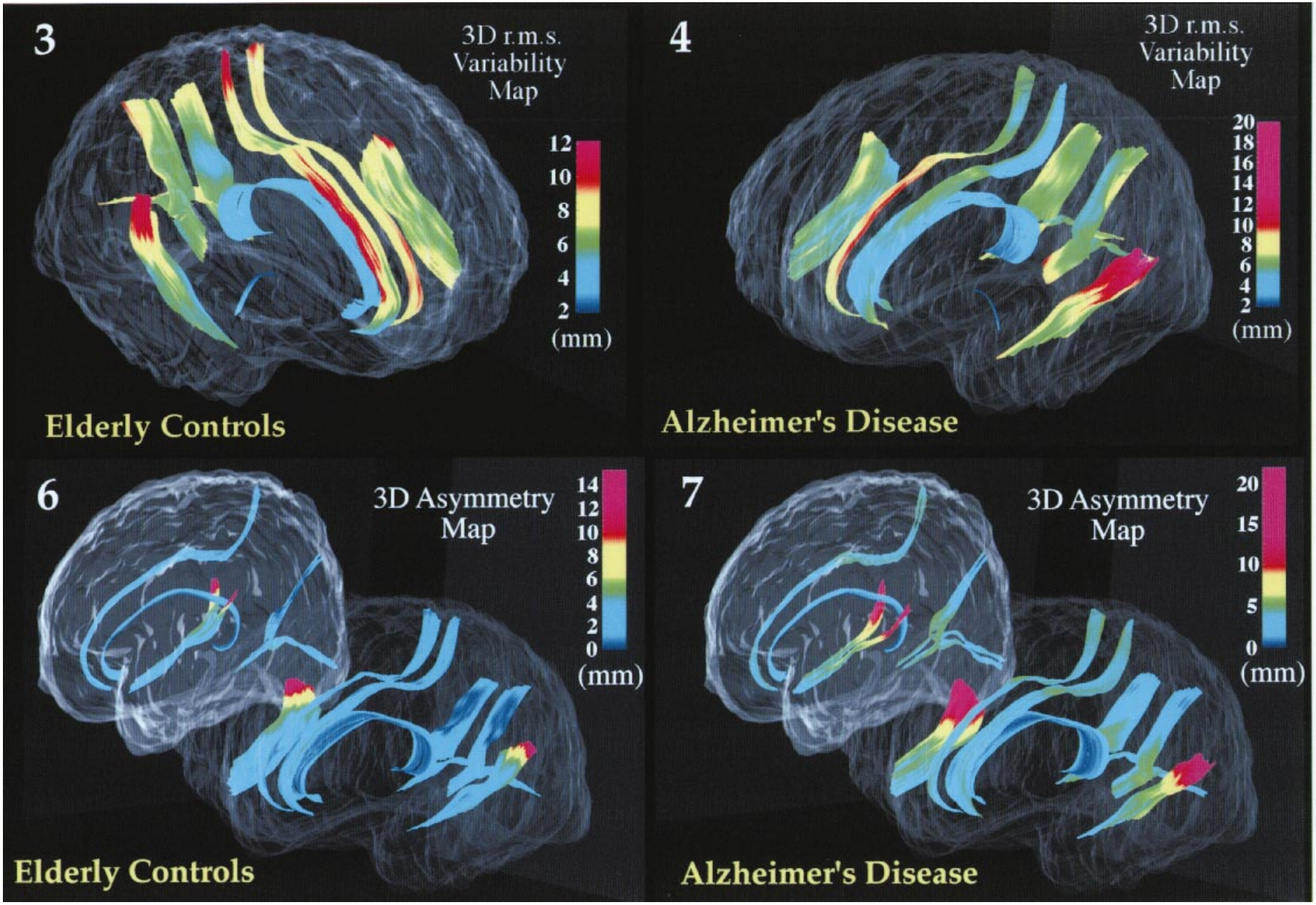
3
3D r.m.s. Variability Map
12
10
8
6
4
2
(mm)
Elderly Controls
4
3D r.m.s. Variability Map
20
18
16
14
12
10
8
6
4
2
(mm)
Alzheimer's Disease
6
3D Asymmetry Map
14
12
10
8
6
4
2
0
(mm)
Elderly Controls
7
3D Asymmetry Map
20
15
10
5
0
(mm)
Alzheimer's Disease

These data are consistent with the emerging hypothesis that AD pathology severely and asymmetrically disrupts temporo-parietal anatomy (Loewenstein *et al.*, 1989; Capitani *et al.*, 1990; Wahlund *et al.*, 1993; Siegel *et al.*, 1996; Corder *et al.*, 1997). Underlying atrophy and left greater than right degeneration of the perisylvian region may widen the Sylvian fissure, introducing additional individual variation and asymmetry superimposed on that already seen in normal aging (Figs 4, 7). This hypothesis is further corroborated by the observations that all structures displayed a slightly higher degree of asymmetry in AD than in controls. In the AD patient group there was negligible asymmetry (0.0–2.5 mm) at the callosal surface and a profile of mild asymmetry values for parieto-occipital, anterior and posterior calcarine and cingulate sulci (0.8–5.7, 2.2–5.9, 1.2–4.4 and 3.3–6.0 mm respectively) which contrasted sharply with the severe asymmetry of the Sylvian fissure (2.3–21.8 mm).

Mapping of Regionally Selective Atrophy at the Corpus Callosum

The next objective was to test the hypothesis that a local or diffuse atrophy of bilaterally connected brain regions might induce secondary effects on homotopically distributed fibers in the corpus callosum (CC). The cross-section of the CC at the interhemispheric plane was digitally subdivided into five distinct sectors of equal rostral extent along the AC–PC axis (Duara *et al.*, 1991; see Fig. 10, top panel). To control for potential effects introduced by stereotaxic normalization, all subsequent analyses were performed first by digitally mapping structure models back into the original, unscaled MRI data. Rigid body (non-scaling; translation and rotation) transformations were, however, still performed to register the brains. When areas of specific sectors were compared between groups, the posterior midbody zone was of particular interest, since fibers crossing in this area selectively innervate the temporo-parietal regions at risk for early neuronal loss in AD (Brun and Englund, 1981).

Consistent with this hypothesis, a severe and significant reduction in the posterior midbody area was found in AD relative to controls, reflecting a dramatic 24.5% decrease from 98.0 ± 8.6 mm^2 in controls to 74.0 ± 5.3 mm^2 in AD ($P < 0.025$; Fig. 8). By contrast, the terminal sectors (1 and 5) of the callosum, corresponding to fibers crossing in the rostrum and splenium respectively, did not undergo a significant areal reduction, with almost identical values in the control and patient group of 160.9 ± 9.6 and 158.6 ± 14.3 mm^2 respectively for the rostral sector ($P > 0.1$), and 148.7 ± 8.6 and 150.8 ± 6.8 mm^2 respectively for the splenial sector ($P > 0.1$). An observed 16.6% mean areal loss in AD for the central sector showed only a trend toward significance ($P < 0.1$), and an apparent 13.4% depression in mean anterior midbody area was statistically insignificant ($P > 0.1$) because of substantial inter-group overlap in the values of these parameters. [To investigate effects of the stereotaxic transform, all analyses were re-performed on the individual surface data in Talairach stereotaxic space; precisely the same pattern of results was found, with a significant posterior midbody area reduction in AD ($P < 0.025$), suggesting that this effect persists even after correction of individual data for differences in brain size and inter-commissural distance.]

Selective changes in the CC accompanying AD pathology were measured by partitioning midsagittal sector outlines into upper and lower sectors; local variability maps (Fig. 9) and average boundary representations (Fig. 10) were then made for the callosum in both subject groups. In both control and AD subjects, sectors showed a distinctly heterogeneous profile of

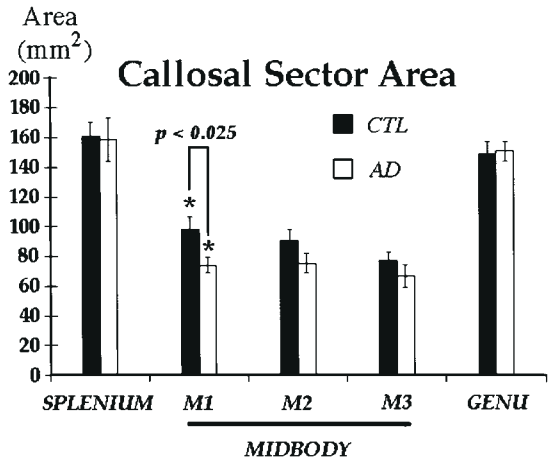

Figure 8. Regionally selective atrophy at the corpus callosum in AD. Areas of specific callosal sectors are shown (as mean values ± SEMs) in control subjects (black bars; $n = 10$) and Alzheimer's patients (white bars; $n = 10$). The partitioning scheme digitally divides the cross-section of the CC at the interhemispheric plane into five distinct sectors of equal rostral extent along the AC–PC axis (Duara *et al.*,1991). Figure 10 (top panel) shows this partition, which divides the callosal midbody into three sectors (here M1–M3). Notice the severe 24.5% decrease in the area of posterior midbody sector M1 from 98.0 ± 8.6 mm^2 in controls to 74.0 ± 5.3 mm^2 in AD ($P < 0.025$). Sectors which approximately represent the genu and splenium are comparatively resilient. As found in Biegon *et al.* (1994), Black *et al.* (1996) and Kaufer *et al.* (1997), however, total callosal area was not found to be significantly depressed in AD (mean ± SD: 525.9 ± 116.8 mm^2) relative to controls (575.4 ± 108.8 mm^2; $P > 0.05$). As a further caveat against the use of total callosal area as a diagnostic index in AD, striking areal variations were observed in both controls (range: 419–810 mm^2) and AD patients (387–812 mm^2). Discrimination based on this parameter alone may therefore be highly unreliable. Despite the 10 times greater image resolution used in this study, and the careful controlling for age, gender, educational level and handedness, both the mean values and range of callosal area values documented here are in strong agreement with prior MR studies of callosal size based on 10 mm-thick sections (Biegon *et al.*, 1994).

variability (Fig. 9*a*,*b*), with confidence limits on 2D variation at the midsagittal plane varying from an SD of 2.0–3.3 mm at the inferior splenium, central midbody and genu to 4.6–5.0 mm at the posterior aspect of the rostrum. Intriguingly, in the posterior midbody zone, where a significant area reduction was apparent in AD, the average callosal representations showed a slight reduction in thickness in AD relative to controls (Fig. 10, lower panel). In addition, a pronounced inflection in shape was demonstrated towards the inferior limit. This feature can be seen in Fig. 10 (lower panel), at stereotaxic location (0.0,–25.0,19.0). This morphology has also been observed in studies of callosal shape in schizophrenia (DeQuardo *et al.*, 1996; Bookstein, 1997).

Sulcal Surface Extent, Area, Curvature and Complexity in Three Dimensions

Anterior–posterior, vertical and lateral extents were determined for sulcal surfaces both before and after transformation of the associated brain images into Talairach stereotaxic space. To examine any effects introduced by stereotaxic transformation of individual data (Talairach and Tournoux, 1988), surface models of structures were digitally mapped back into the unscaled original MRI data. A simple rigid body transformation was then applied to the images and surface models to vertically orient the interhemispheric plane and horizontally orient the AC–PC line. Native extents of structures (i.e. their true anatomic extents before stereotaxic transformation) along the three coordinate axes are shown graphically in Figure 11*a*–*c*. The anterior–

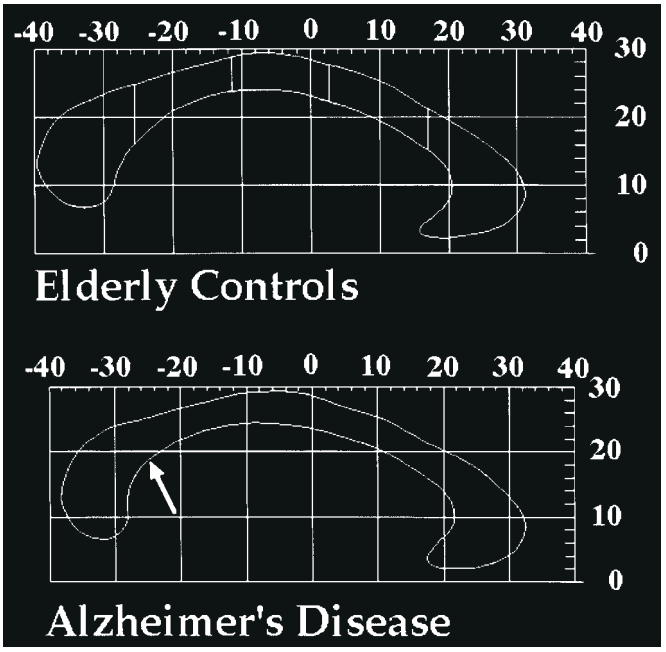

Figure 10. Midsagittal corpus callosum in elderly normal subjects and AD: average boundary representation and partitioning scheme. Average boundary representations of the midsagittal callosum in normal controls and Alzheimer's patients indicate a mild reduction in thickness in AD relative to controls, accompanied by a pronounced inflection in shape (white arrow) in the neighborhood of stereotaxic location (0.0,–25.0,19.0).The overlying posterior midbody sector (the second of five, top panel) underwent a 24.5% reduction in area in AD compared with controls ($P < 0.025$).

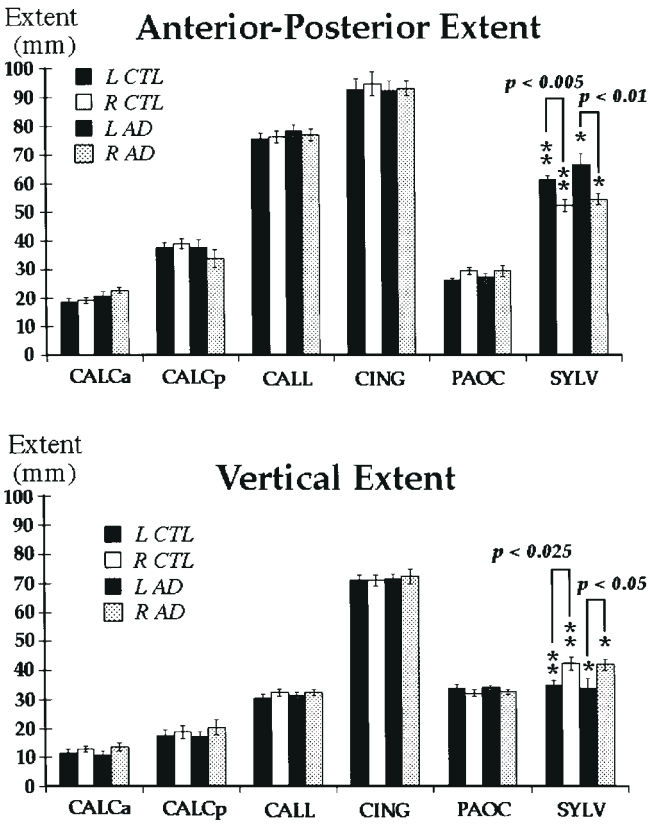

Figure 11. Spatial extents of major sulci in both brain hemispheres. Extents of major sulci in both brain hemispheres and both subject groups are reported (as mean values ± SEMs) prior to stereotaxic normalization. In both normal controls (uniform bars) and AD (stippled bars) marked Sylvian fissure asymmetries are observed, with rostral extents being greater on the left, and vertical extents greater on the right (cf. Figs 6, 7, 12).

posterior extent of the Sylvian fissure was significantly greater on the left than the right both in the control group (61.1 ± 1.4 mm, left hemisphere; 52.3 ± 2.1 mm, right hemisphere; $P < 0.005$) and in AD (66.4 ± 3.7 mm, left; 54.4 ± 1.8 mm, right; $P < 0.01$). Conversely, the native vertical extents of the Sylvian fissure were significantly greater on the right than on the left in controls (34.7 ± 1.8 mm, left; 42.3 ± 2.4 mm, right; $P < 0.025$) and in AD (33.7 ± 3.4 mm, left; 42.1 ± 1.9, right; $P < 0.05$). After the stereotaxic transformation selectively removed the contribution of brain size to sulcal variation, the Sylvian fissure asymmetries achieved an even greater level of significance. The resulting stereotaxic extents, along the anterior–posterior axis, were then observed to be considerably greater on the left than on the right in controls (58.5 ± 1.3 mm, left; 49.2 ± 1.7 mm, right; $P < 0.0005$) and in AD subjects (64.3 ± 3.8, left; 51.2 ± 1.6 mm, right; $P < 0.005$). Again, stereotaxic vertical extents followed the pattern of being greater on the right than the left in controls (36.1 ± 6.5 mm, left; 43.8 ± 2.4 mm, right; $P < 0.02$) and in AD (34.0 ± 3.1 mm, left; 43.0 ± 2.1, right; $P < 0.025$). Furthermore, the stereotaxic transformation revealed that Sylvian fissure length asymmetries resulted from positional asymmetries of the caudal tip of the fissure rather than the rostral tip, which exhibited no significant asymmetries in either subject group (Fig. 12*a–c*; see also the asymmetry maps shown in Figs 6, 7). No asymmetries were found in the lateral extent of the Sylvian fissure ($P > 0.05$), and no other structure displayed asymmetries for any structural parameter ($P > 0.05$). Lateral extents, not addressed in prior stereotaxic studies, indicated the extreme depth of the parieto-occipital sulci and Sylvian fissures (Table 5). These sulci had mean lateral extents of 11.4–12.6 and 15.2–15.5 mm respectively in controls and similar values in the AD group, with slightly higher values for both groups after stereotaxic transformation. The AD group did not have significantly increased lateral extents, relative to controls, for any of the sulci measured, which might have been expected given their deep lateral course and the known effects of sulcal widening in AD (Gado *et al.*, 1982).

Surface Area Measures

Three-dimensional surface area measures for all structures, both before and after stereotaxic transformation, are shown in Table 6. Native area measures for controls ranged from mean hemispheric values of 1.1–1.4 and 3.2–3.4 cm^2 for the anterior and posterior calcarine sulci respectively, increasing to 4.5–5.2 and 7.1–8.0 cm^2 for the parieto-occipital and supracallosal sulci, and reaching 8.7–10.1 and 9.3–9.4 cm^2 for the cingulate sulci and Sylvian fissure respectively. No disease-specific differences were apparent, nor were there any inter-hemispheric asymmetries in structure area for either subject group, suggesting that the positional and shape asymmetries of the Sylvian fissure area not accompanied by hemispheric differences in the absolute area of its surface.

Surface Curvature

Normalized curvature indices revealed striking differences in sulcal morphology. Native curvature values in controls ranged from (1.084 ± 0.009, left; 1.098 ± 0.015, right) for the comparatively flat anterior calcarine sulcus, to a peak value of 2.340 ± 0.081 (left; 2.292 ± 0.088, right) for the highly curved

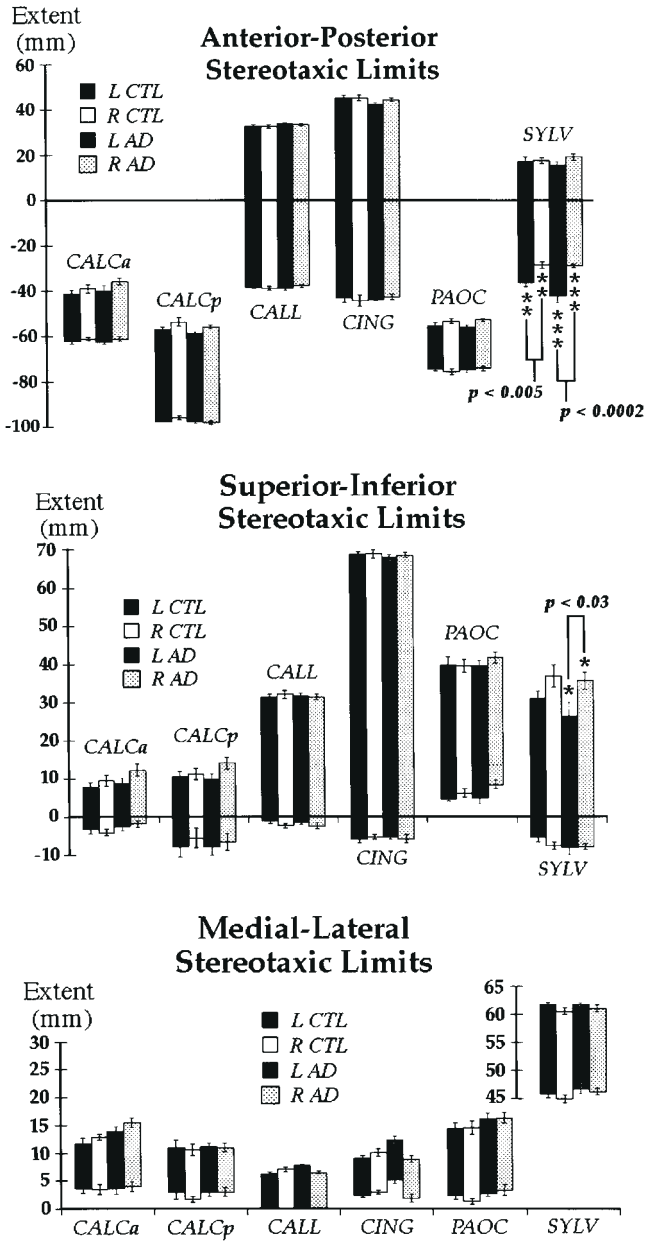

Figure 12. Confidence limits for structure location in Talairach stereotaxic space. Stereotaxic transformation revealed that Sylvian fissure length asymmetries resulted from positional asymmetries of the caudal tip of the fissure rather than the rostral tip, which exhibited no significant asymmetries in either subject group. Lateral extents (lower panel), not addressed in prior stereotaxic studies, indicated the extreme depth of the parieto-occipital sulci and Sylvian fissures, with slightly higher values for both groups after stereotaxic transformation. Interestingly, the AD group did not have significantly increased lateral extents, relative to controls, for any of the sulci measured, which might have been expected given their deep lateral course and the known effects of sulcal widening in AD.

Table 5
Surface complexity of deep structures in normal aging and AD: fractal dimension and lateral extent measures in left (L) and right (R) hemispheres

Structure	Controls	AD
Fractal dimension		
CALCa	(L) 2.1388 ± 0.0013	2.1393 ± 0.0028
	(R) 2.1393 ± 0.0017	2.1338 ± 0.0008
CALCp	(L) 2.1537 ± 0.0065	2.1643 ± 0.0054
	(R) 2.1504 ± 0.0033	2.1643 ± 0.0076
CALL	(L) 2.2030 ± 0.0035	2.1907 ± 0.0053
	(R) 2.1976 ± 0.0032	2.1886 ± 0.0041
CING	(L) 2.1921 ± 0.0052	2.1921 ± 0.0047
	(R) 2.2050 ± 0.0068	2.2013 ± 0.0029
PAOC	(L) 2.1485 ± 0.0030	2.1574 ± 0.0066
	(R) 2.1540 ± 0.0060	2.1592 ± 0.0042
SYLV	(L) 2.1417 ± 0.0013	2.1431 ± 0.0018
	(R) 2.1429 ± 0.0017	2.1406 ± 0.0019
Lateral extent (mm)		
CALCa	(L) 7.75 ± 1.40	8.55 ± 5.52
	(R) 9.20 ± 1.63	11.25 ± 6.13
CALCp	(L) 8.05 ± 1.33	8.10 ± 2.00
	(R) 8.70 ± 2.45	7.95 ± 2.59
CALL	(L) 6.05 ± 1.06	7.50 ± 1.07
	(R) 6.85 ± 1.50	6.20 ± 1.55
CING	(L) 6.20 ± 1.17	6.80 ± 1.91
	(R) 6.70 ± 1.78	6.60 ± 2.11
PAOC	(L) 11.50 ± 3.30	12.85 ± 2.65
	(R) 12.80 ± 3.54	13.45 ± 3.48
SYLV	(L) 15.80 ± 1.29	15.65 ± 3.46
	(R) 15.50 ± 3.08	14.70 ± 3.03

Fractal dimension is an extremely compact measure of surface complexity, condensing all surface shape details into a single numeric value which summarizes the irregularity of the sulcal course inside the brain. Briefly, the measure reflects the rate at which the surface area of the sulcus increases as the scale of measurement is reduced. Severe decreases in the fractal dimension of the cerebral cortex have been reported in epilepsy (Cook *et al.*, 1994), so we hypothesized that a similar reduction might occur in AD, specifically in the perisylvian zones at risk of selective atrophy in early AD. No such reductions were found, either between subject groups or between brain hemispheres. Analysis of additional cortical areas may be necessary to further validate this finding. Characteristic ranges for the surface complexity of specific sulci, as well as confidence limits on surface variation, may prove useful as geometric invariants when designing computerized strategies which distinguish one sulcal type from another (MacDonald *et al.*, 1997). Lateral extent measures are also shown (as mean values ± SEMs) for the selected sulci, prior to stereotaxic normalization. By contrast with Figure 11, Sylvian fissure asymmetries were not found for the lateral extent data, nor were differences found between dementia patients and elderly controls for either of these parameters.

supracallosal sulcus. A curvature value of 1.0 indicates a flat, planar structure. The characteristically curved, 'Λ-shaped' morphology of the posterior calcarine sulcus was reflected in its mean curvature indices (1.169 ± 0.038, left; 1.133 ± 0.012, right), which were higher than corresponding values for the anterior segment of the calcarine sulcus (1.084 ± 0.009, left; 1.093 ± 0.014, right). The elaborate curved morphology of the cingulate sulcus, as it arches round the limbic system, was indicated by its elevated curvature indices (1.442 ± 0.045, left; 1.486 ± 0.045, right). The 3D course of the Sylvian fissure was also found to be significantly more curved on the right (1.184 ± 0.029) than on the left (1.109 ± 0.014) in controls ($P < 0.025$). This effect, however, showed only a trend towards significance in AD (1.104 ± 0.015, left; 1.138 ± 0.016, right; $P < 0.1$).

Analysis of curvature data both before and after stereotaxic normalization revealed a further effect of the Talairach stereotaxic system: in control subjects, the mean curvature index of the corpus callosum increased by 7.9% on the left and 7.7% on the right as a result of the stereotaxic transformation. Similar increases (of 5.1% on the left, 5.0% on the right) were introduced in the AD group. The increase in the amount of 'arching' exhibited by the callosum probably stems from contracting the AC–PC distance in the individual MRI datasets to a reference value of 23.5 mm. As noted earlier, this standard AC–PC distance is significantly smaller ($P < 0.05$) than the mean intercommissural distances obtained for each subject group.

Fractal Dimension and Surface Complexity

Differences in sulcal morphology were also revealed by fractal dimension analysis (Table 5), which reflects the rate at which sulcal surface area increases as the scale of measurement is reduced. Low complexity values of 2.13–2.14 were determined

Table 6
Three-dimensional surface area measures for deep sulcal surfaces in aging and AD

Structure	Controls (cm^2)	AD (cm^2)
Left hemisphere		
CALCa	1.118 ± 0.121	1.632 ± 0.295
	(1.213 ± 0.128)‡	(1.818 ± 0.366)
CALCp	3.184 ± 0.246	3.449 ± 0.563
	(3.455 ± 0.254)	(3.500 ± 0.391)
CALL	7.060 ± 0.397	8.583 ± 0.433
	(7.265 ± 0.366)	(8.697 ± 0.410)
CING	8.704 ± 0.459	9.533 ± 0.768
	(9.021 ± 0.455)	(9.826 ± 0.896)
PAOC	4.513 ± 0.475	5.283 ± 0.563
	(4.844 ± 0.436)	(5.507 ± 0.442)
SYLV	9.368 ± 0.262	9.610 ± 0.636
	(9.184 ± 0.300)	(9.419 ± 0.561)
Right hemisphere		
CALCa	1.353 ± 0.116	2.058 ± 0.406
	(1.480 ± 0.123)	(2.253 ± 0.464)
CALCp	3.407 ± 0.342	3.575 ± 0.534
	(3.759 ± 0.385)	(3.711 ± 0.465)
CALL	8.020 ± 0.676	7.274 ± 0.831
	(8.290 ± 0.673)	(7.259 ± 0.600)
CING	10.086 ± 1.024	9.496 ± 0.914
	(10.377 ± 0.980)	(9.936 ± 1.086)
PAOC	5.188 ± 0.610	5.506 ± 0.695
	(5.567 ± 0.592)	(5.716 ± 0.480)
SYLV	9.294 ± 0.572	8.507 ± 0.536
	F(9.086 ± 0.446)	(8.397 ± 0.519)

Surface area measures are shown (as mean ± SEMs) for deep anatomical surfaces in normal elderly subjects and Alzheimer's patients, both *before* (first value) and *after* (‡: value in parentheses) digital transformation into Talairach stereotaxic space. Note that, as expected from an analysis of Table 3, the stereotaxic transformation marginally increases the internal surface area of the occipital and paralimbic sulci, and that this increase is slightly more pronounced in the AD patients than in controls. By contrast, the surface area of the deep Sylvian fissure is marginally reduced in both subject groups by the stereotaxic transformation, especially in controls. This is because most of the Sylvian surface falls in the central sector of stereotaxic space. Statistics determined in Tables 2 and 3 suggest that this central sector is generally subjected to a rostro-caudal contraction, so that the anterior and posterior commissures can fall at their canonically defined coordinate locations (Talairach and Tournoux, 1988). No disease-specific differences were apparent ($P > 0.05$), nor were there any inter-hemispheric asymmetries in structure area for either subject group ($P > 0.05$), suggesting that the positional and shape asymmetries of the Sylvian fissure area not accompanied by hemispheric differences in the absolute area of its surface.

for the relatively planar anterior calcarine sulcus, in sharp contrast with values exceeding 2.19–2.20 for the cingulate sulcus (in both hemispheres). Consistent with this observation, we noted qualitatively that the elaborate intracerebral course of the cingulate often demonstrated multiple highly variable branching patterns, which may or may not connect with other accessory, paralimbic sulci (cf. Ono *et al.*, 1990; Paus *et al.*, 1996a,b). Complexity values also tended to fall in a characteristic range for each type of sulcus (Table 5), but were surprisingly stable across subjects and groups.

Contouring Reliability

As in our earlier cryosection studies (Thompson *et al.*, 1996a), the reliability of the contouring process itself was evaluated by repeatedly delineating the same structure and comparing the data obtained in multiple trials. Since the 20 MR scans had specifically been acquired at high resolution (1-mm-thick MR slices, with a 0.9765 × 0.9765 mm in-plane pixel resolution and no inter-slice gap), it was important to determine whether the advantages of this protocol would actually be reflected in reduced contouring error.

All sulcal surfaces in the left hemisphere of a single, randomly selected brain were manually outlined six times, in random order. Outlines were converted to parametric mesh form, and

Table 7
Effects of contouring error on 3D extent and surface area parameters

Structure	Anterior–posterior extent (mm)	Vertical extent (mm)	Lateral extent (mm)	Surface area (cm^2)
PAOC	23.91 ± 0.31 (1.30%)	38.61 ± 0.46 (1.19%)	13.0 ± 0.0 (0%)[a]	5.563 ± 0.022 (0.40%)
CALCa	23.49 ± 0.46 (1.96%)	10.33 ± 0.28 (2.71%)	9.0 ± 0.0 (0%)	1.192 ± 0.012 (1.01%)
CALCp	43.11 ± 0.28 (0.65%)	22.32 ± 0.13 (0.60%)	10.0 ± 0.0 (0%)	5.242 ± 0.018 (0.34%)
CALL	77.29 ± 0.26 (0.33%)	28.61 ± 0.16 (0.55%)	7.5 ± 0.0 (0%)	8.272 ± 0.018 (0.22%)
CING	86.02 ± 0.32 (0.37%)	72.60 ± 0.19 (0.26%)	7.0 ± 0.0 (0%)	9.414 ± 0.015 (0.16%)
SYLV	51.10 ± 0.20 (0.39%)	42.38 ± 0.26 (0.61%)	15.5 ± 0.0 (0%)	9.064 ± 0.030 (0.33%)

This table summarizes the differences which occurred in outlining the same structure, in the left hemisphere of a randomly selected control subject, on multiple occasions ($n = 6$). All studies of morphometric variation across subjects incorporate identification errors as a source of variability. Errors due to differences in structure delineation in multiple trials are broken down by structure. For each structure, mean measures and their standard deviations are given; SDs are also expressed as a percentage of the corresponding mean values.

[a]Identification error is not isotropic, as outlines were made for a particular structure in all the sagittal sections in which that structure could be distinguished. Selected structures could be distinguished in the same sections in each trial, partly because the interhemispheric vault or the lateral aspect of the insula provided the medial limit for each sulcus, and their lateral limits were not ambiguous. In-plane differences in structure delineation, however, were introduced across multiple trials, and these contributed to differences in the surface areas, as well as the vertical and rostral extents, of each individual structure.

Table 8
Effects of contouring error on curvature, 3D stereotaxic variability and fractal dimension measures

Structure	Curvature	Nodal deviation r.m.s. (mm)	Fractal dimension
PAOC	1.1047 ± 0.0033 (0.30%)	0.316 ± 0.083 [0.250 ± 0.095]‡	2.1475 ± 0.0005 (0.023%)
CALCa	1.0829 ± 0.0048 (0.44%)	0.251 ± 0.064 [0.190 ± 0.082]	2.1393 ± 0.0007 (0.033%)
CALCp	1.2955 ± 0.0031 (0.24%)	0.361 ± 0.118 [0.235 ± 0.064]	2.1882 ± 0.0013 (0.059%)
CALL	1.9316 ± 0.0079 (0.41%)	0.435 ± 0.143 [0.341 ± 0.136]	2.2053 ± 0.0012 (0.054%)
CING	1.2838 ± 0.0022 (0.17%)	0.429 ± 0.150 [0.378 ± 0.165]	2.1693 ± 0.0005 (0.023%)
SYLV	1.1503 ± 0.0036 (0.31%)	0.373 ± 0.137 –	2.1585 ± 0.0011 (0.051%)

As in Table 7, this table provides a further analysis of the differences which occurred in outlining the same structure, in the left hemisphere of a randomly selected normal subject, on multiple occasions ($n = 6$). Meshes were constructed from the outlines produced in different trials, and the nodal deviation r.m.s. measures summarize the 3D spatial discrepancies in the stereotaxic locations of their grid points, across the series of trials. For each structure, mean measures and their SDs are given; SDs are also expressed as a percentage of the corresponding mean values. ‡For purposes of comparison, values in square brackets denote identically calculated error values obtained (for the five sulci examined) in our previous study of sulcal variability, in which ultra-high-resolution 3D cryosection images of the human brain were analyzed (Thompson *et al.*, 1996a). The low error values in both studies suggest that contouring error represented a negligible fraction of the overall measures of inter-subject variability.

the full range of geometric parameters were calculated for each surface. Results of these tests are presented in Tables 7 and 8. While all measures were stable across the series of trials, curvature and fractal dimension measures were the most robust – worst case errors represented 0.44 and 0.059% of the corresponding mean values for these measures in the control group (q.v., CALCa/p: Table 8). Standard errors for repeated measures of extent and area data were, in the worst cases, only 0.46 mm and 0.030 cm^2 respectively (q.v., CALCa and PAOC: Table 7). The effects of contouring errors on each geometric variable were, in all cases but two, between 9 and 190 times smaller than the corresponding variation in the same quantity

across each group of subjects. The worst case occurred when measuring the variability in curvature and fractal dimension, for the anterior calcarine sulcus (CALCa). A 'floor effect' occurred because inter-subject variability was very small, in this case, but the measures of variability (across the 10 subjects in each group) were still six times greater than the contouring error.

The regional impact of identification error and hand jitter during manual outlining was assessed in greater detail by creating additional 3D variability maps for the repeated contouring trials (n = 6), showing local profiles of contouring error across each structure. Fig. 13*a* shows an example of such an error map for the three occipital sulci in the left hemisphere of the selected brain. Contouring error across trials was smallest for the rather flat anterior branch of the calcarine sulcus (mean nodal deviation: 0.251 ± 0.064 mm). This compared with a slightly higher error of 0.361 ± 0.118 mm for the posterior branch, 0.316 ± 0.083 mm and 0.373 ± 0.137 mm for the parieto-occipital sulcus and Sylvian fissure, and 0.435 ± 0.143 mm and 0.429 ± 0.150 mm for the callosal and cingulate sulci respectively.

Discussion

Two general principles emerge from the broad spectrum of neuroanatomic maps and indices examined here. First, population-based averaging and comparative analysis of digital anatomic maps in normal aging and AD suggested a range of global and local disease-related differences. Confidence limits on 3D cortical variation in controls showed a marked increase from 2–4 mm at the callosum to a peak of 12–13 mm at the external cerebral surface. In AD, however, while variability was marginally higher than in controls at the callosal surface, the variability across the surface of the Sylvian fissure rose extremely sharply, from an SD of 6.0 mm rostrally to 19.6 mm caudally on the left and from 5.0 mm rostrally to 9.0 mm caudally on the right. Although there is a substantial literature on Sylvian fissure cortical surface asymmetries (Eberstaller, 1884; Cunningham, 1892; Geschwind and Levitsky, 1968; Davidson and Hugdahl, 1994) and their relation to functional lateralization (Strauss *et al.*, 1983), handedness (Witelson and Kigar, 1992), language function (Davidson and Hugdahl, 1994), asymmetries of asssociated cytoarchitectonic fields (Galaburda and Geschwind, 1981) and their thalamic projection areas (Eidelberg and Galaburda, 1982), no prior report exists mapping the spatial profile of asymmetries in 3D space. When Sylvian fissure asymmetries were mapped in three dimensions, the marked rostral and vertical extent asymmetries in controls (left posterior limit 9.7 mm more caudal than right; $P < 0.0005$) were severely increased in AD (left limit 16.6 mm more caudal than right; $P < 0.0002$), and between-hemisphere differences in the anterior–posterior position of the Sylvian fissure's posterior limit were also found to be significantly greater in AD than in matched controls ($P < 0.05$). Local maps (Figs 6, 7) also revealed a sharp rise in 3D asymmetry in AD, reaching 21.8 mm at the posterior limit of the left Sylvian fissure, compared with 15.4 mm in controls. Greater variability of the left perisylvian surface and greater Sylvian fissure asymmetry in AD suggests that AD pathology asymmetrically disrupts the anatomy of the temporo-parietal cortex. In AD, Sylvian fissure CSF volume has also been shown to rise, relative to controls, more sharply on the left than the right [left volume 31.5% higher in AD than controls ($P < 0.02$; n = 32) but right volume only 20.4% higher ($P < 0.09$; Wahlund *et al.*, 1993)]. Underlying atrophy and possible left greater than right degeneration of perisylvian gyri may widen the Sylvian fissure, superimposing additional individual variation and asymmetry on that already seen in normal aging (Figs 4, 7). Significant left greater than right metabolic dysfunction and cognitive impairment have been reported in both PET (Loewenstein *et al.*, 1989; Siegel *et al.*, 1996) and neuropsychiatric (Capitani *et al.*, 1990) studies of AD, and in PET studies of related amnestic disorders (Corder *et al.*, 1997). Recent PET studies have also examined cognitively normal subjects who are 'at risk' for AD in the sense that they experience mild memory complaints and have at least two relatives with AD (Small *et al.*, 1995). Left greater than right metabolic impairment also appears in these subjects, and the deficit has been shown to be significantly more asymmetric in at-risk subjects carrying the apolipoprotein type 4 allele (ApoEε4; a risk factor for familial AD) relative to those subjects without ApoEε4 (Small *et al.*, 1995). Accentuated patterns of structural asymmetry and variation found here in AD support these findings, suggesting either that (i) the left hemisphere is more susceptible than the right to neurodegeneration in AD; or that (ii) left hemispheric impairment results in greater structural change and lobar metabolic deficits (Loewenstein *et al.*, 1989).

A second principle evident from this study is the anatomically specific relationship observed between putative fiber loss in callosal regions and the dynamic progression of cortical and lobar atrophy characteristic of AD. Size reduction and shape inflection were observed in commissural regions that map association areas at risk of selective metabolic loss and incipient atrophy in early stages of AD (Figs 8, 10). Greater resilience was observed in splenial sectors, which map the parieto-occipital and calcarine surfaces which are comparatively resistant to neuronal loss in AD (Pearson *et al.*, 1985). Severe and regionally selective areal loss and focal shape inflection in the posterior callosal midbody may reflect disease-related disruption of the commissural system connecting bilateral temporal and parietal cortical zones, since these regions are known to be at risk for early metabolic dysfunction, perfusion deficits and selective neuronal loss in AD (DeCarli *et al.*, 1996). Any focal or diffuse abnormalities of bilaterally connected cortical regions may be expected to have secondary effects on homotopically distributed fibers in the callosum (Biegon *et al.*, 1994), which serves as the primary cortical projection system, and consists of ~200–350 million fibers in man (Aboitiz *et al.*, 1992). Effects on regional callosal structure have been reported in schizophrenia (Woodruff *et al.*, 1995; DeQuardo *et al.*, 1996), attention deficit hyperactivity disorder (Giedd *et al.*, 1994; Baumgardner *et al.*, 1996), relapsing–remitting multiple sclerosis (Pozzilli *et al.*, 1991), AD (Hofmann *et al.*, 1995; Vermersch *et al.*, 1996; Janowsky *et al.*, 1996) and multi-infarct dementia (Yoshii *et al.*, 1990).

Controversy exists over whether different callosal regions undergo selective changes in aging and dementia (Yoshii *et al.*, 1990), and even whether effects in dementia are significant compared with age-matched controls (Biegon *et al.*, 1994). As found in Biegon *et al.* (1994), Black *et al.* (1996) and Kaufer *et al.* (1997), we did not find the total callosal area to be significantly depressed in AD (mean ± SD: 525.9 ± 116.8 mm^2) relative to controls (575.4 ± 108.8 mm^2; $P > 0.05$). These values (determined prior to stereotaxic normalization) are in broad agreement with, but marginally higher than, previously determined callosal area values (Biegon *et al.*, 1994) of 562 ± 98 mm^2 in elderly controls (n = 13; MR slice thickness: 10 mm; age: 64.8 ± 9.0 years) and 480 ± 133 mm^2 in AD ($P > 0.05$; n = 20; age: 70.1 ± 7.4 years, with slightly lower MMSE scores of 17 ± 7.2 and

a range of 9–25). Both our data and those of Biegon *et al.* (1994), Black *et al.* (1996) and Kaufer *et al.* (1997) do not fully agree with earlier reports that total callosal area discriminated between AD and control subjects (Hofmann *et al.*, 1995; $P < 0.05$), and that combined callosal area was significantly reduced in AD [by 7.0% relative to controls; $P < 0.05$ (Yoshii *et al.*, 1994)]. If selective AD-related atrophy occurs in specific callosal sectors (Black *et al.*, 1996) when areas of these sectors are pooled with that of other more robust regions, they may or may not be significantly reduced, depending on disease severity.

The finding that the same highly circumscribed site at the callosum (Figs 8, 10) shows a comparable shape inflection in schizophrenia (DeQuardo *et al.*, 1996; Bookstein, 1997) is intriguing. Due to differences in the etiology of the two diseases, fiber deficiency at this site in schizophrenia may be associated with a neurodevelopmental disruption of the sulco-gyral organization of temporal lobe fibers that cross in this region (Kikinis *et al.*, 1994). In AD, however, a similarly localized fiber deficiency may result from temporo-parietal neuronal loss, associated with the early perfusion and cognitive performance deficits in AD. It is well-known that a massive perinatal loss of callosal axons, lasting from the 35th gestational week to the end of the first postnatal month (Clarke *et al.*, 1989; La Mantia and Rakic, 1990) leads to a restricted pattern of adult callosal connections, but controversy exists over whether callosal area is further reduced in normal aging relative to young normal controls (Biegon *et al.*, 1994; cf. Doraiswamy *et al.*, 1991). Callosal area reductions in AD may have functional significance, as smaller partial callosal size often reflects a focal decrease in the number of small diameter (<3 mm) fibers (Aboitiz *et al.*, 1992) or decreased myelin deposition, associated with decreased conduction velocity and longer interhemispheric transmission times. These and other callosal studies, interpreted in the context of (i) the temporo-parietal perfusion deficits and temporal neuronal loss typical in early AD, and (ii) correlations between reduced association cortex metabolism and cognitive performance, suggest that neuronal loss and white matter abnormalities in AD may partially exert their effect through disruption of long cortico-cortical pathways (DeCarli *et al.*, 1996). Earlier reports of CC alterations in clinically mild AD (Hofmann *et al.*, 1995; Janowsky *et al.*, 1996; Vermersch *et al.*, 1996) support these observations and further highlight the selective vulnerability of callosal regions in AD.

Extreme variations in cortical patterns, as quantified by this study, also suggest that caution may be necessary in using the Talairach stereotaxic system to support cross-subject and cross-group comparisons of cortically derived events or functional maps. Three-dimensional stereotaxic localization is widely accepted by the neuroscience community not only as a framework for coordinate-based morphometry, multi-modality brain mapping and neurosurgical studies (Talairach and Szikla, 1967; Burzaco, 1985; Missir *et al.*, 1989; Steinmetz *et al.*, 1989, 1990; Vannier *et al.*, 1991; Mazziotta *et al.*, 1995), but also as a quantitative system of reference in functional imaging studies. Direct digital subtraction of stereotaxic functional maps in dementia studies may lead to spurious results, since homologous cortical regions in different subjects may not be brought into register. Since stereotaxic systems differ significantly in their capacity to compensate for inter-subject variations in the anatomy of the brain (Burzaco, 1985), cortical variation maps may serve as a metric to directly evaluate different stereotaxic systems, and to compare their effectiveness in reconciling inter-subject variations. Confounding effects of highly variable cortical patterns can be reduced in multi-subject functional studies by employing image registration strategies which fluidly deform the sulcal patterns of different subjects into structural correspondence (Davatzikos, 1996; Thompson and Toga, 1996, 1997, 1998; Drury *et al.*, 1997). These fluid maps encode information on complex variations in sulcal topography in human populations, enabling cross-subject transfer, comparison and integration of functional data from many subjects. Fluid transformations of cortical maps have recently allowed inter-species comparison of cytoarchitecture (Van Essen *et al.*, 1997), construction of a population-based digital brain atlas (Thompson

Figure 5. Three-dimensional variability maps for occipital lobe sulci in aging, AD and *post mortem* digital cryosection imaging. Variability maps for major sulci of the occipital lobe, in several population subgroups, reveal cross-modality effects on measures of 3D cortical variation. Separate occipital lobe variability maps were constructed from the MRI data acquired from (top left) control subjects ($n = 10$); (top right) patients with AD ($n = 10$); and (bottom left) normal elderly brains ($n = 6$) imaged immediately *post mortem* by ultra-high-resolution digital cryosection imaging (Thompson *et al.*, 1996a). In each case, an oblique right-hand side view is shown which illustrates the course of the parieto-occipital sulcus from its antero-ventral junction with the medial surface of the calcarine sulcus, which it divides into anterior and posterior segments. The posterior calcarine sulcus is shown joining it inferiorly. Notice the pronounced increase in variability, in every case, towards the exterior occipital surface. Peak variability values, however, differ substantially between the two imaging modalities. High cortical variability, observed in 3D MRI, is compounded in *post mortem* studies by additional factors which affect specimen integrity (e.g. cryoprotection, CSF loss and fixation). These factors require computational strategies which selectively remove anatomical variance at the cortex, in order to compare and correlate histochemical maps with functional maps derived *in vivo* from multiple subjects, groups and imaging modalities (Drury *et al.*, 1997; Mega *et al.*, 1997; Thompson and Toga, 1997).

Figure 9. Midsagittal corpus callosum in elderly normal subjects and AD. Separate maps of local variability were constructed for (*a*) control subjects and (*b*) Alzheimer's patients, expressing (in color) the r.m.s. variation of callosal points in each subject group around an average boundary representation of the callosum at the midsagittal plane of Talairach stereotaxic space. Unlike all other maps in this study, these are strictly 2D maps, since the midsagittal analysis of callosal morphology is conducted in a single vertical plane. Average boundary representations have therefore been thickened for visualization purposes only. Two trends are apparent. Although the variability measure peaks at the inferior genu, this may be an artifact, due to the difficulties of defining an unambiguous anatomical limit for the inferior aspect of the genu. Nevertheless, the pronounced rise in variability at the rostral midbody in AD (*b*) may reflect disease-related enlargement of the third ventricle, which forms its inferior boundary.

Figure 13. Maps of contouring error for occipital lobe sulci. These error maps show the reliability of structure delineation in multiple trials. Algorithms developed for calculating variability across subjects were used to map out local discrepancies which occurred when contouring the same structure repeatedly ($n = 6$) in a randomly selected brain. Three-dimensional surface models of the parieto-occipital, anterior and posterior calcarine sulci are derived from the left hemisphere of the randomly selected brain. The color encodes the r.m.s. magnitude of the displacement vectors required to map the surface obtained in each trial onto the average of the surfaces obtained in multiple trials. Identically constructed error maps are shown (*b*) for the same occipital lobe sulci, repeatedly traced in six ultra-high-resolution ($1300 \times 1024^2 \times$ 24-bit color) 3D cryosection images of the human brain [data reproduced, for purposes of comparison, from Thompson *et al.* (1996a)]. In conjunction with additional data on the stability of individual geometric parameters measured in multiple trials (Tables 7,8), these tests suggest that the contouring reliability achievable with the high-resolution 3D gradient-echo (spoiled GRASS) MR scans approached that obtainable with ultra-high-resolution cryosection imaging (see Table 8). Variability in delineating sulcal trajectories also represented a negligible fraction of the overall inter-subject variability, which was consistently a factor 9–190 times greater than the errors introduced in the contouring process. Densely acquired 3D gradient-echo scans may therefore offer quantitative advantages in delineating structural anomalies in a variety of disease states.

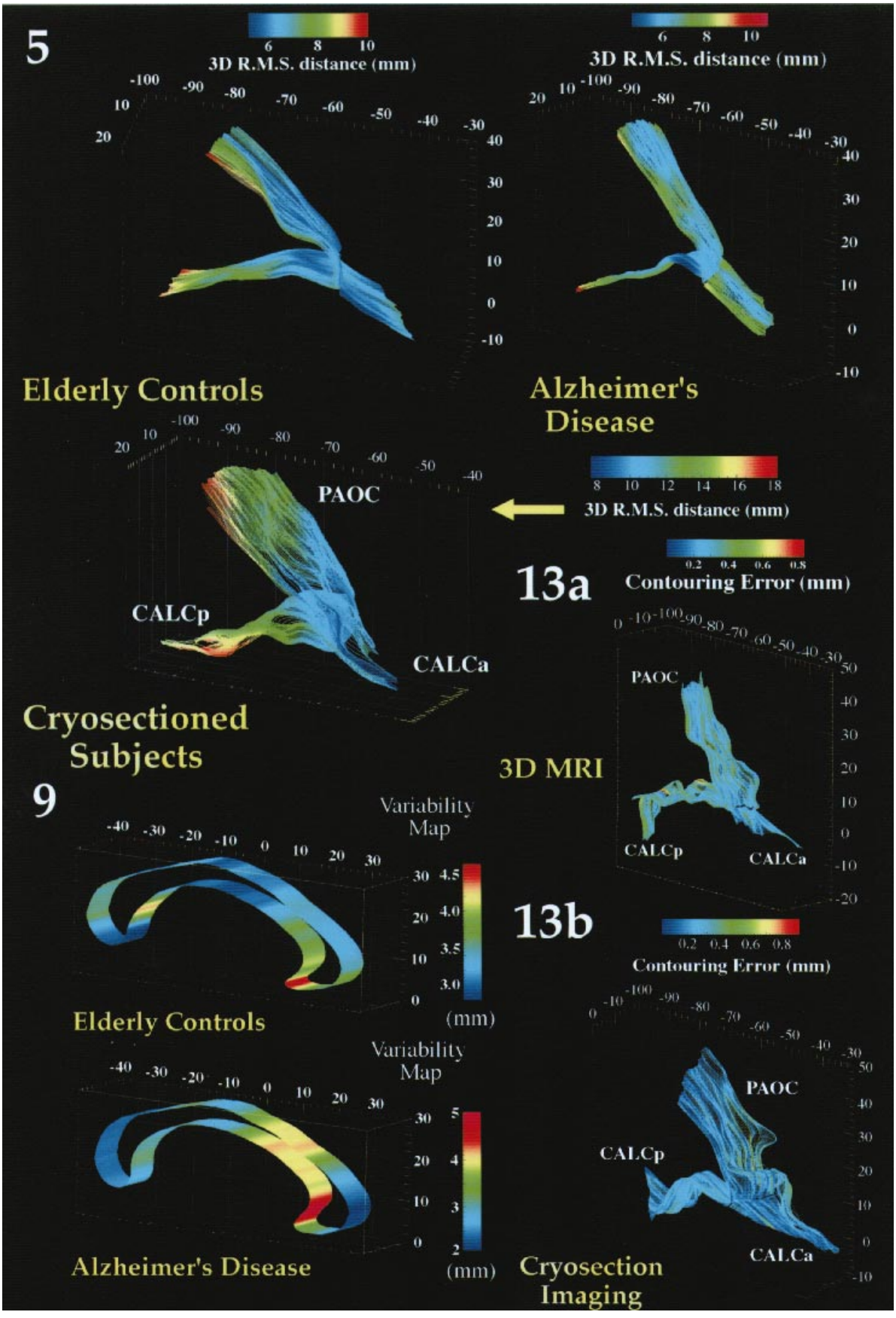
5
6 8 10
3D R.M.S. distance (mm)
Elderly Controls
Alzheimer's Disease
8 10 12 14 16 18
3D R.M.S. distance (mm)
PAOC
CALCp
CALCa
Cryosectioned Subjects
13a
0.2 0.4 0.6 0.8
Contouring Error (mm)
3D MRI
9
Variability Map
Elderly Controls
(mm)
13b
Alzheimer's Disease
Cryosection Imaging

and Toga, 1997), mapping of 4D growth patterns in the developing human brain (Thompson and Toga, 1998) and detection of structural anomalies in AD (Thompson *et al.*, 1997).

The findings presented here on cortical variation and asymmetry in normal aging and AD reveal its regional heterogeneity, local asymmetries and 3D characteristics. Commissural regions at risk of early selective damage are identified, and these sites are found to be topographically linked with known cortical and lobar patterns of structural, metabolic and perfusion deficits. In the future, more advanced strategies for the assessment and quantitative encoding of cortical variation may provide extensive information on differential vulnerability of brain regions, disease-specific variants, and selective changes in callosal and lobar anatomy that accompany aging and AD.

Notes

This work was generously supported by research grants from the National Library of Medicine (LM/MH05639), the National Science Foundation (BIR 93-22434), the NCRR (RR05956) and the Human Brain Project, which is funded jointly by NIMH and NIDA (P20 MH/DA52176). P.M.T. was supported by the United States Information Agency, under Grant G-1-00001, by a Fellowship of the Howard Hughes Medical Institute and by a research grant from the U.S.–U.K. Fulbright Commission, London.

Address correspondence to Dr Arthur W. Toga, Room 4238, Reed Neurological Research Center, Laboratory of Neuro Imaging, 710 Westwood Plaza, Los Angeles, CA 90095-1769, USA. Email: toga@loni.ucla.edu.

References

Aboitiz F, Scheibel AB, Fisher RS, Zaidel E (1992) Fiber composition of the human corpus callosum. Brain Res 598:143–153.

Adams RL, Smigielski J, Jenkins RL (1984) Development of a Satz–Mogel short form of the revised Wechsler Adult Intelligence Scale (WAIS-R) J Consult Clin Psychol 52:908.

Arnold SE, Hyman BT, Flory J, Damasio AR, Van Hoesen GW (1991) The topographical and neuroanatomical distribution of neurofibrillary tangles and neuritic plaques in the cerebral cortex of patients with Alzheimer's Disease. Cereb Cortex 1:103–116.

Baumgardner TL, Singer HS, Denckla MB, Rubin MA, Abrams MT, Colli MJ, Reiss AL (1996) Corpus callosum morphology in children with Tourette syndrome and attention deficit hyperactivity disorder. Neurology 47:477–482.

Biegon A, Eberling JL, Richardson BC, Roos MS, Wong ST, Reed BR, Jagust WJ (1994) Human corpus callosum in aging and Alzheimer's Disease: a magnetic resonance imaging study. Neurobiol Aging 15:393–397.

Black SE, Szekely C, Szalai JP, Kidron D, Yu D, Parker J, Buck B, Stanchev P, Bronskill M (1996) Can MRI brain measures distinguish Alzheimer's Disease from normal aging?, Poster presentation, 2nd International Conference on Functional Mapping of the Human Brain, June 17–21, 1996, Boston, MA. NeuroImage 3:S476.

Blacker D, Albert MS, Bassett SS, Go RC, Harrell LE, Folstein MF (1994) Reliability and validity of NINCDS-ADRDA criteria for Alzheimer's Disease. The National Institute of Mental Health Genetics Initiative. Arch Neurol 51:1198–1204.

Bookstein FL (1997) Landmark methods for forms without landmarks: morphometrics of group differences in outline shape. Med Image Anal 1:225–243.

Braak H, Braak E (1991) Neuropathological staging of Alzheimer-related changes. Acta Neuropathol 82:239–259.

Brun A, Englund E (1981) Regional pattern of degeneration in Alzheimer's Disease: neuronal loss and histopathologic grading. Histopathology 5:549–564.

Burzaco J (1985) Stereotaxic pallidotomy in extrapyramidal disorders. Appl Neurophysiol 48:283–287.

Capitani E, Della Sala S, Spinnler H (1990) Controversial neuropsychological issues in Alzheimer's Disease: influence of onset-age and hemispheric asymmetry of impairment. Cortex 26:133–145.

Clarke S, Kraftsik R, Van der Loos H, Innocenti GM (1989) Forms and measures of adult and developing human corpus callosum: is there sexual dimorphism? J Comp Neurol 280:213–230.

Coleman PD, Flood DG (1987) Neuron numbers and dendritic extent in normal aging and Alzheimer's Disease. Neurobiol Aging 8:521–545.

Cook MJ, Free SL, Fish DR, Shorvon SD, Straughan K, Stevens JM (1994) Analysis of cortical patterns. In: Magnetic resonance scanning and epilepsy (Shorvon SD et al., eds), pp 263–274. New York: Plenum Press.

Corder EH, Jelic V, Basun H, Lannfelt L, Valind S, Winblad B, Nordberg A (1997) No difference in cerebral glucose metabolism in patients with Alzheimer Disease and differing apolipoprotein E genotypes. Arch Neurol 54:273–277.

Cressie NAC (1991) Statistics for spatial data. New York: Wiley.

Cuénod CA, Denys A, Michot JL, Jehenson P, Forette F, Kaplan D, Syrota A, Boller F (1993) Amygdala atrophy in Alzheimer's Disease: an *in vivo* magnetic resonance imaging study. Arch Neurol 50:941–945.

Cummings J, Benson DF, LoVerme S (1980) Reversible dementia. Illustrative cases, definition, and review. J Am Med Assoc 243: 2434–2439.

Cunningham DJ (1892) Contribution to the surface anatomy of the cerebral hemispheres. Cunningham Mem (R Irish Acad) 7:372.

Davatzikos C (1996) Spatial normalization of 3D images using deformable models. J Comput Assist Tomogr 20:656–665.

Davatzikos C, Vaillant M, Resnick SM, Prince JL, Letovsky S, Bryan RN (1996) A computerized approach for morphological analysis of the corpus callosum. J Comput Assist Tomogr 20:88–97.

Davidson RJ, Hugdahl K (1994) Brain asymmetry. Boston, MA: MIT Press.

Davis PC, Mirra SS, Alazraki N (1994) The brain in older persons with and without dementia: findings on MR, PET and SPECT images. Am J Radiol, 162:1267–1278.

DeCarli C, Grady CL, Clark CM, Katz DA, Brady DR, Murphy DG, Haxby JV, Salerno JA, Gillette JA, Gonzalez-Aviles A, Rapoport SI (1996) Comparison of positron emission tomography, cognition, and brain volume in Alzheimer's disease with and without severe abnormalities of white matter. J Neurol Neurosurg Psychiat 60:158–167.

Delaère P, Duyckaerts C, Brion JP, Poulain V, Hauw JJ (1989) Tau, paired helical filaments and amyloid in the neocortex: a morphometric study of 15 cases with graded intellectual status in aging and senile dementia of Alzheimer type. Acta Neuropathol (Berl) 77:645–653.

DeQuardo JR, Bookstein FL, Green WD, Brunberg JA, Tandon R (1996) Spatial relationships of neuroanatomic landmarks in schizophrenia. Psychiat Res 67:81–95.

Doraiswamy PM, Figiel GS, Husain MM, McDonald WM, Shah SA, Boyko OB, Ellinwood EH Jr, Krishnan KR (1991) Aging of the human corpus callosum: magnetic resonance imaging in normal volunteers. J Neuropsychiat Clin Neurosci 3:392–397.

Di Patre PL (1990) Cytoskeletal alterations might account for the phylogenetic vulnerability of the human brain to Alzheimer's disease. Med Hypoth 34:165–170.

Drury HA, Van Essen DC, Snyder AZ, Shulman GL, Akbudak E, Ollinger JM, Conturo TE, Raichle M, Corbetta M (1997) Warping fMRI activation patterns onto the visible man atlas using fluid deformations of cortical flat maps. 3rd International Conference on Functional Mapping of the Human Brain, Copenhagen, May 19–23 1997. NeuroImage 5:S421.

Duara R, Kushch A, Gross-Glenn K, Barker WW, Jallad B, Pascal S, Loewenstein DA, Sheldon J, Rabin M, Levin B (1991) Neuroanatomic differences between dyslexic and normal readers on magnetic resonance imaging scans. Arch Neurol 48:410–416.

Eberstaller O (1884) Zür Oberflachen Anatomie der Grosshirn Hemisphaeren. Wien Med Bl 7:479, 642, 644.

Eidelberg D, Galaburda AM (1982) Symmetry and asymmetry in the human posterior thalamus: I. Cytoarchitectonic analysis in normal persons. Arch Neurol 39(6):325–332.

Erkinjuntti T, Lee DH, Gao F, Steenhuis R, Eliasziw M, Fry R, Merskey H, Hachinski VC (1993) Temporal lobe atrophy on magnetic resonance imaging in the diagnosis of early Alzheimer's disease. Arch Neurol 50:305–310.

Folstein MF, Folstein SE, McHugh PR (1975) 'Mini mental state': a practical method of grading the cognitive state of patients for the clinician. J Psychiat Res 12:189–198.

Fox PT (1995) Spatial normalization: origins, objectives, applications and alternatives (Editorial). Hum Brain Map 3:161–164.

Friedland RP, Luxenberg J (1988) Neuroimaging and dementia. In: Clinical neuroimaging: frontiers in clinical neuroscience (Theodore WH, ed), vol. 4, pp 139–163. New York: Alan R Liss.

Friedland RP, Budinger TF, Jagust WJ, Koss E, Derenzo S, Huesman RH,

Yano Y (1985) Positron tomography and the differential diagnosis and pathophysiology of Alzheimer's disease. In: Senile dementia of the Alzheimer type (Traber J, Gispen WH, eds), pp 124–133. Heidelberg: Springer-Verlag.
Gado M, Hughes CP, Danziger W, Chi D, Jost G, Berg L (1982) Volumetric measurements of the cerebrospinal fluid spaces in demented subjects and controls. Radiology 144:535–538.
Galaburda AM (1995) Anatomic basis of cerebral dominance. In: Brain asymmetry (Davidson RJ, Hugdahl K, eds), pp 51–73. Boston, MA: MIT Press.
Geschwind N, Levitsky W (1968) Human brain: left–right asymmetries in temporal speech region. Science 161:186.
Galaburda AM, Geschwind N (1981) Anatomical asymmetries in the adult and developing brain and their implications for function. Adv Pediatr 28:271–292.
Galaburda AM, Sanides F, Geschwind N (1978) Human brain: cytoarchitectonic left–right asymmetries in the temporal speech region. Arch Neurol 35:812–817.
Giedd JN, Castellanos FX, Casey BJ, Kosuch P, King AC, Hamburger SD, Rapoport JL (1994) Quantitative morphology of the corpus callosum in attention deficit hyperactivity disorder. Am J Psychiat 151: 665–669.
Gómez-Isla T, Price JL, McKeel DW, Morris JC, Growdon JH, Hyman B (1996) Profound loss of layer II entorhinal cortex neurons occurs in very mild Alzheimer's disease. J Neurosci 16:4491–4500.
Grenander U, Miller MI (1994) Representations of knowledge in complex systems. J Royal Statist Soc B, 56:549–603.
Griffen LD (1994) The intrinsic geometry of the cerebral cortex. J Theor Biol 166:261–273.
Hofmann E, Becker T, Meixensberger J, Jackel M, Schneider M, Reichmann H (1995) Disturbances of cerebrospinal fluid (CSF) circulation — neuropsychiatric symptoms and neuroradiological contribution. J Neural Transm Gen Sect 99:79–88.
Hynd GW, Hall J, Novey ES, Eliopulos D, Black K, Gonzales JJ, Edmonds JE, Riccio C, Cohen M (1995) Dyslexia and corpus callosum morphology. Arch Neurol 52:32–38.
Janowsky JS, Kaye JA, Carper RA (1996) Atrophy of the corpus callosum in Alzheimer's disease versus healthy aging. J Am Geriatr Soc 44:798–803.
Jernigan TL, Salmon DP, Butters N, Hesselink JR (1991) Cerebral structure on MRI: Part I. Localization of age-related changes. Biol Psychiat 29:55–67.
Kaplan E, Goodglass H, Weintraub S (1984) The Boston naming test. Philadelphia, PA: Lea & Phebiger Press.
Katzman R (1986) Alzheimer's disease. N Engl J Med 314:964.
Kaufer DI, Miller BL, Itti L, Fairbanks LA, Li J, Fishman J, Kushi J, Cummings JL (1997) Midline cerebral morphometry distinguishes frontotemporal dementia and Alzheimer's disease/ Neurology 48:978–985.
Khachaturian ZS (1985) Diagnosis of Alzheimer's disease. Arch Neurol 42: 1097–1105.
Kido DK, Caine ED, LeMay M, Ekholm S, Booth H, Panzer R (1989) Temporal lobe atrophy in patients with Alzheimer disease: a CT study. Am J Neuro Rep 7:551–555.
Kikinis R, Shenton ME, Gerig G, Hokama H, Haimson J, O'Donnell BF, Wible CG, McCarley RW, Jolesz FA (1994) Temporal lobe sulco-gyral pattern anomalies in schizophrenia: an *in vivo* MR three-dimensional surface rendering study. Neurosci Lett 182:7–12.
Killiany RJ, Moss MB, Albert MS, Sandor T, Tieman J, Jolesz F (1993) Temporal lobe regions on magnetic resonance imaging identify patients with early Alzheimer's disease. Arch Neurol 50:949–954.
LaMantia AS, Rakic P (1990) Axon overproduction and elimination in the corpus callosum of the developing rhesus monkey. J Neurosci 10:2156–2175.
Larsen JP, Høien T, Ödegaard H (1992) Magnetic resonance imaging of the corpus callosum in developmental dyslexia. Cogn Neuropsychol 9:123–134.
Leonard CM (1996) Structural variation in the developing and mature cerebral cortex: noise or signal? In: Developmental neuroimaging: mapping the development of brain and behavior (Thatcher RW, Reid Lyon G, Rumsey J, Krasnegor N, eds), pp 207–231. San Diego, CA: Academic Press.
Lezak M (1983) Neuropsychological assessment (2nd edn). New York: Oxford University Press.
Loewenstein DA, Barker WW, Chang JY, Apicella A, Yoshii F, Kothari P, Levin B, Duara R (1989) Predominant left hemisphere metabolic dysfunction in dementia. Arch Neurol 46:146–152.
MacDonald D, Venugopal R, Caramanos Z, Petrides M, Avis D, Evans AC (1997) A surface-based 2D sulcal atlas. 3rd International Conference on Functional Mapping of the Human Brain, Copenhagen, May 19–23 1997. NeuroImage 5:S414.
Mathalon DH, Sullivan EV, Rawles JM, Pfefferbaum A (1993) Correction for head size in brain-imaging measurements. J Psychiat Res: Neuroimag 50:121–139.
Mazziotta JC, Toga AW, Evans AC, Fox PT, Lancaster J (1995) A probabilistic atlas of the human brain: theory and rationale for its development. NeuroImage 2:89–101.
McKhann G, Drachman D, Folstein M, Katzman R, Price D, Stadian EM (1984) Clinical diagnosis of Alzheimer's disease: report of the NINCDS-ARDRA Work Group under the auspices of the Health and Human Services Task Force on Alzheimer's Disease. Neurology 34:939–944.
Mega MS, Chen S, Thompson PM, Woods RP, Karaca TJ, Tiwari A, Vinters H, Small GW, Toga AW (1997) Mapping pathology to metabolism: coregistration of stained whole brain sections to PET in Alzheimer's disease. NeuroImage 5:147–153.
Meltzer CC, Frost JJ (1994) Partial volume correction in emission-computed tomography: focus on Alzheimer disease. in: Functional neuroimaging: technical foundations (Thatcher RW, Hallett M, Zeffiro T, John ER, Huerta M, eds), pp 163–170. San Diego, CA: Academic Press.
Missir O, Dutheil-Desclercs C, Meder JF, Musolino A, Fredy D (1989) Central sulcus patterns at MRI. Neuroradiology 16:133–144.
Murphy DGM, DeCarli CD, Daly E, Gillette JA, McIntosh AR, Haxby JV, Teichberg D, Schapiro MB, Rapoport SI, Horwitz B (1993) Volumetric magnetic resonance imaging in men with dementia of the Alzheimer type: correlations with disease severity. J Biol Psychiat 34:612–621.
Ono M, Kubik S, Abernathey CD (1990) Atlas of the cerebral sulci. Stuttgart: Georg Thieme Verlag.
Osterreith PA (1944) Le Teste de Copie d'une Figure Complexe. Arch Psychol 30:206–256.
Pandya DN, Seltzer B (1986) The topography of commisural fibers. In: Two hemispheres–one brain: functions of the corpus callosum (Lepore F, Ptito M, Jasper HH, eds), p 47. New York: Alan R Liss.
Paus T, Tomaiuolo F, Otaky N, MacDonald D, Petrides M, Atlas J, Morris R, Evans AC (1996a) Human cingulate and paracingulate sulci: pattern, variability, asymmetry and probabilistic map. Cereb Cortex 6: 207–214.
Paus T, Otaky N, Caramanos Z, MacDonald D, Zijdenbos A, D'Avirro D, Gutmans D, Holmes CJ, Tomaiuolo, Evans AC (1996b) *In vivo* morphometry of the intrasulcal gray matter in the human cingulate, paracingulate, and superior-rostral sulci: hemispheric asymmetries, gender differences and probability maps. J Comp Neurol 376: 664–673.
Pearson RC, Esiri MM, Hiorns RW, Wilcock GK, Powell TP (1985) Anatomical correlates of the distribution of the pathological changes in the neocortex in Alzheimer disease. Proc Natl Acad Sci USA 82:4531–4534.
Pozzilli C, Bastianello S, Padovani A, Passafiume D, Millefiorini E, Bozzao L, Fieschi C (1991) Anterior corpus callosum atrophy and verbal fluency in multiple sclerosis. Cortex 27:441–445.
Rademacher J, Caviness VS Jr., Steinmetz H, Galaburda AM (1993) Topographical variation of the human primary cortices: implications for neuroimaging, brain mapping and neurobiology. Cereb Cortex 3:313–329.
Rajkowska G, Goldman-Rakic P (1995) Cytoarchitectonic definition of pre-frontal areas in the normal human cortex. II. Variability in locations of areas 9 and 46 and relationship to the Talairach coordinate system. Cereb Cortex 5:323–337.
Rey A (1941) L'Examen Psychologique dans les cas d'Encephalopathie Traumatique. Arch Psychol 28:286–340.
Roland PE, Zilles K (1994) Brain atlases — a new research tool. Trends Neurosci 17:458–467.
Sanides F (1962) Die Architektonik des menschlichen Stirnhirns. In: Monographien aus dem Gesamtegebiete der Neurologie und Psychiatrie 98 (Mueller M, Spatz H, Vogel P, eds). Berlin: Springer-Verlag.
Scott SA (1993) Dendritic atrophy and remodeling of amygdaloid neurons in Alzheimer's disease. Dementia 4:264–272.
Siegel BV Jr, Shihabuddin L, Buchsbaum MS, Starr A, Haier RJ, Valladares

Neto DC (1996) Gender differences in cortical glucose metabolism in Alzheimer's disease and normal aging. J Neuropsychiat Clin Neurosci 8:211–214.
Small GW, Mazziotta JC, Collins MT, Baxter LR, Phelps ME, Mandelkern MA, Kaplan A, La Rue A, Adamson CF, Chang L et al. (1995) Apolipoprotein E type 4 allele and cerebral glucose metabolism in relatives at risk for familial Alzheimer disease J Am Med Assoc 273:942–947.
Steinmetz H, Furst G, Freund H-J (1989) Cerebral cortical localization: application and validation of the proportional grid system in MR imaging. J Comput Assist Tomogr 13:10–19.
Steinmetz H, Furst G, Freund H-J (1990) Variation of perisylvian and calcarine anatomic landmarks within stereotaxic proportional coordinates. Am J Neuroradiol 11:1123–1130.
Stensaas SS, Eddington DK, Dobelle WH (1974) The topography and variability of the visual cortex in man. J Neurosurg 40:747–755.
Stoyan D, Stoyan H (eds) (1991) Fractals, random shapes, and point fields: methods of geometric statistics. New York: Wiley.
Strauss E, Kosaka B, Wada J (1983) The neurobiological basis of lateralized cerebral function. A review. Hum Neurobiol 2:115–127.
Talairach J, Szikla G (1967) Atlas d'Anatomie Stereotaxique du Telencephale: Etudes Anatomo-Radiologiques. Paris: Masson & Cie.
Talairach J, Tournoux P (1988) Co-planar stereotaxic atlas of the human brain. New York: Thieme Medical Publishers.
Tanna NK, Kohn MI, Horwich DN, Jolles PR, Zimmerman RA, Alves WM, Alavi A (1991) Analysis of brain and cerebrospinal fluid volumes with MR imaging: impact on PET data correction for atrophy: Part II: Aging and Alzheimer dementia. Radiology 178:109–114.
Thompson PM, Toga AW (1996) A surface-based technique for warping 3-dimensional images of the brain. IEEE Trans Med Imag 15:1–16.
Thompson PM, Toga AW (1997) Detection, visualization and animation of abnormal anatomic structure with a deformable probabilistic brain atlas based on random vector field transformations. Med Image Anal 1:271–294.
Thompson PM, Toga AW (1998) Anatomically-driven strategies for brain image warping and pathology detection. In: Brain warping (Toga AW, ed.). San Diego, CA: Academic Press.
Thompson PM, Schwartz C, Lin RT, Khan AA, Toga AW (1996a) 3D statistical analysis of sulcal variability in the human brain. J Neurosc 16:4261–4274.
Thompson PM, Schwartz C, Toga AW (1996b) High-resolution random mesh algorithms for creating a probabilistic 3D surface atlas of the human brain. NeuroImage 3:19–34.
Thompson PM, MacDonald D, Mega MS, Holmes CJ, Evans AC, Toga AW (1997) Detection and mapping of abnormal brain structure with a probabilistic atlas of cortical surfaces. J Comput Assist Tomogr 21:567–581.
Van Essen DC, Drury HA, Joshi SC, Miller MI (1997) Comparisons between human and macaque using shape-based deformation algorithms applied to cortical flat maps. 3rd International Conference on Functional Mapping of the Human Brain, Copenhagen, May 19–23 1997. NeuroImage 5:S41.
Vannier MW, Brunsden BS, Hildebolt CF, Falk D, Cheverud JM, Figiel GS, Perman WH, Kohn LA, Robb RA, Yoffie RL, Bresina SJ (1991) Brain surface cortical sulcal lengths: quantification with three-dimensional MR imaging. Radiology 180:479–484.
Vermersch P, Roche J, Hamon M, Daems-Monpeurt C, Pruvo JP, Dewailly P, Petit H (1996) White matter magnetic resonance imaging hyperintensity in Alzheimer's disease: correlations with corpus callosum atrophy. J Neurol 243:231–234.
Wahlund LO, Andersson-Lundman G, Basun H, Almkvist O, Bjorksten KS, Saaf J, Wetterberg L (1993) Cognitive functions and brain structures: a quantitative study of CSF volumes on Alzheimer patients and healthy control subjects. Magn Reson Imag 11:169–174.
Watson JDG, Myers R, Frackowiak RSJ, Hajnal JV, Woods RP, Mazziotta JC, Shipp S, Zeki S (1993) Area V5 of the human brain: evidence from a combined study using positron emission tomography and magnetic resonance imaging. Cereb Cortex 3:79–94.
Wechsler D (1955) Wechsler Adult Intelligence Scale. New York: The Psychological Corp.
West MJ, Coleman PD, Flood DG, Troncoso JC (1994) Differences in the pattern of hippocampal neuronal loss in normal aging and Alzheimer's disease. Lancet 344:769–772.
Whitehouse PJ, Price DL, Clark AW, Coyle JT, DeLong MR (1981) Alzheimer's disease: evidence for selective loss of cholinergic neurons in the nucleus basalis. Ann Neurol 10:122–126.
Wilcock GK, Esiri MM (1982) Plaques, tangles and dementia: a quantitative study. J Neurol Sci 56:343–356.
Witelson SF (1989) Hand and sex difference in the isthmus and genu of the corpus callosum: a post mortem morphological study. Brain 112:799–835.
Witelson SF, Kigar DL (1992) Sylvian fissure morphology and asymmetry in men and women: bilateral differences in relation to handedness in men. J Comp Neurol 323:326–340.
Witelson SF, Glezer II, Kigar DL (1995) Women have greater density of neurons in posterior temporal cortex. J Neurosci 15:3418–3428.
Woodruff PW, McManus IC, David AS (1995) Meta-analysis of corpus callosum size in schizophrenia. J Neurol Neurosurg Psychiat 58:457–461.
Woods RP (1996) Modeling for intergroup comparisons of imaging data. NeuroImage 4:84–94.
Yoshii F, Shinohara Y, Duara R (1990) Cerebral white matter bundle alterations in patients with dementia of Alzheimer type and patients with multi-infarct dementia — magnetic resonance imaging study. Rinsho Shinkei 30:110–112.